

EMPIRICAL BOLOMETRIC FLUXES AND ANGULAR DIAMETERS OF 1.6 MILLION TYCHO-2 STARS AND RADII OF 350,000 STARS WITH GAIA DR1 PARALLAXES

DANIEL J. STEVENS¹, KEIVAN G. STASSUN^{2,3}, B. SCOTT GAUDI^{1,4}

¹The Ohio State University, Department of Astronomy, 140 W. 18th Ave., Columbus, OH 43210, USA

²Vanderbilt University, Department of Physics & Astronomy, 6301 Stevenson Center Ln., Nashville, TN 37235, USA

³Fisk University, Department of Physics, 1000 17th Ave. N., Nashville, TN 37208, USA

⁴Jet Propulsion Laboratory, California Institute of Technology, 4800 Oak Grove Dr., Pasadena, CA 91109, USA

ABSTRACT

We present bolometric fluxes and angular diameters for over 1.6 million stars in the *Tycho-2* catalog, determined using previously-determined empirical color-temperature and color-flux relations. We vet these relations via full fits to the full broadband spectral energy distributions for a subset of benchmark stars, and perform quality checks against the large set of stars for which spectroscopically-determined parameters are available from LAMOST, RAVE, and/or APOGEE. We then estimate radii for the 355,502 *Tycho-2* stars in our sample whose *Gaia* DR1 parallaxes are precise to $\lesssim 10\%$. For the 64,960 of these stars with external spectroscopic information, we achieve median uncertainties on the effective temperatures, bolometric fluxes, angular diameters, and radii of 1.0%, 1.4%, 2.4%, and 7.5%, respectively. For the 290,542 remaining stars, we achieve median uncertainties of 0.9%, 1.3%, 2.2%, and 7.5%, respectively. These stellar parameters are shown to be reliable for stars with $T_{\text{eff}} \lesssim 7000$ K. The over half a million bolometric fluxes and angular diameters presented here will serve as an immediate trove of empirical stellar radii with the *Gaia* second data release, at which point effective temperature uncertainties will dominate the radius uncertainties. Already, dwarf, subgiant, and giant populations are readily identifiable in our purely empirical luminosity-effective temperature (theoretical) Hertzsprung-Russell diagrams.

1. INTRODUCTION

Measurements of stellar radii are paramount to our understanding of stellar evolution. Different physical prescriptions in stellar evolution models for, e.g., winds, mass-loss, and convective overshoot, predict different masses and radii for stars of the same mass, age, and metallicity. Similarly, stars with different elemental abundance ratios will have significantly different evolutionary paths in the luminosity-effective temperature plane, even if they have the same mass and overall metal abundance. Thus, placing precise constraints on these parameters are our only way of constraining the wide range of plausible stellar evolution models.

For example, in sparsely populated areas of the Hertzsprung-Russell (HR) diagram – e.g., the Hertzsprung gap, wherein massive ($M_{\text{ZAMS}} \gtrsim 1.5 M_{\odot}$) stars have ceased core hydrogen fusion but have not yet ignited hydrogen fusion in their shells – stellar evolution models are poorly constrained. Thus improving the precision with which we measure the fundamental parameters of the few stars in these regimes provides us with the most promising way of constraining short-lived phases of stellar evolution.

To date, double-lined eclipsing binaries and stars with angular radii measured interferometrically and distances measured by parallax provide the most robustly determined model-independent stellar radii. The canonical Torres et al. (2010) sample contains double-lined eclipsing binaries (and α Centauri A and B) with masses and radii determined to

$< 3\%$, but their sample contains only four M dwarfs. Birkby et al. (2012) lists a few dozen M dwarfs in eclipsing binaries or with radii known from interferometry, but the radius uncertainty for this sample is as large as 6.4%. Interferometry provides radii (via angular diameters) to $\sim 1.5\%$ for AFG stars (Boyajian et al. 2012a) and $\sim 5\%$ for K and M dwarfs (Boyajian et al. 2012b), but this technique is limited to very bright (and thus nearby) stars. Among young, low-mass pre-main-sequence stars, there is a severe paucity of benchmark-quality eclipsing binaries, limiting empirical tests of star formation and evolution models (e.g., Stassun et al. 2014a).

This paucity of precise radius measurements for isolated low-mass stars hinders our ability to make progress on several long-standing puzzles. For example, there is strong evidence that magnetic activity affects the structure of low-mass stars. Measured K and M dwarf radii have been shown to exceed model-predicted radii at fixed T_{eff} by 10-15% (cf. Mann et al. 2015; Birkby et al. 2012). This “radius inflation” problem of K- and M-dwarfs has yet to be fully captured in stellar models (see, e.g., Stassun et al. 2012; Somers & Stassun 2016, and references therein).

The solution to the aforementioned problems is twofold: we must increase the sample of stars for which radii are empirically measured, and we must improve the precision and accuracy of these radius measurements. This requires precise parallaxes; *Gaia* DR1 (Gaia Collaboration 2016; Gaia Collaboration et al. 2016) provides astrometry at roughly the precision of *Hipparcos*, including parallaxes, but for about two

million bright stars (Lindegren et al. 2016), as compared to the roughly 100,000 stars in the Hipparos catalog (Perryman et al. 1997). To obtain similarly precise radii, we must know the effective temperatures and bolometric fluxes to high precision as well; moreover, we now also need to know the extinction to high precision, since assuming zero extinction for stars outside the immediate solar neighborhood introduces an uncertainty that is now non-negligible in comparison to the uncertainties in the other quantities.

A methodology for determining empirical radii of stars has been demonstrated by Stassun et al. (2016) for some 500 planet-host stars, in which empirical measurements of stellar bolometric fluxes and temperatures permitted determination of accurate, empirical angular diameters, which with the *Gaia* DR1 parallaxes permitted accurate and empirical measurement of the stellar radii. Extending this approach to a much larger sample of stars across the entire sky would be of great value in particular for improving the selection of promising targets for the upcoming *TESS* (Ricker et al. 2015) and *PLATO* (Rauer et al. 2014) missions, which rely on accurate estimates of stellar radii and other parameters to optimize the target samples for finding small transiting planets (see Stassun et al. 2014b; Campante et al. 2016; Stassun et al. 2017).

So motivated, we present estimated extinctions, effective temperatures, bolometric fluxes (and thus angular diameters), for over 1.6 million *Tycho-2* stars. We also present radii for 355,502 of these stars that have *Gaia* DR1 parallaxes with reported precisions of less than 10%. In Section 2.1, we describe the broad-band flux measurements we use to derive the temperatures and bolometric fluxes as well as the spectroscopic parameters that we adopt as priors. In Section 3, we describe the iterative method for de-reddening the literature magnitude measurements and obtaining effective temperatures and bolometric fluxes, and we furthermore validate the method against a large subset of stars with spectroscopic parameter determinations. As the fundamental products of this work, we present our bolometric fluxes, as well as angular and physical radii, in Section 4. In Section 5, we compare our radii and effective temperatures to the T_{eff} -radius relation of Boyajian et al. (2012b) and note the limitations of our technique. Finally, we conclude with a summary of our results and the expected improvements that will be possible with future *Gaia* data releases in Section 6.

2. DATA

We begin with the *Tycho-2* catalog as our base sample, providing ~ 2 million stars with B_T and V_T magnitudes as well as astrometry that the *Gaia* team has used to provide parallaxes in its first data release (DR1). In this section, we describe the additional catalogs and other literature sources that we combine with the *Tycho-2* base catalog to form our study sample. A summary of the parent sample and the various subsamples employed in this work is provided in Table 1.

2.1. Literature Photometry

We queried VizieR (Ochsenbein et al. 2000) for photometry in the U , B and V bands from Mermilliod (2006); in

Strömgren b and y from Pauzen (2015); in B_T and V_T from the *Tycho-2* catalog (Høg et al. 2000); and in J , H , and K_S from the Two-Micron All Sky Survey (2MASS; Skrutskie et al. 2006, Cutri et al. 2003). We queried by *Tycho-2* ID, taking the closest match that lied within $0.1'$ of the VizieR-calculated sky position. We excluded stars *Tycho* stars that appear in the original *Tycho* catalog but not in the *Tycho-2* catalog, and we exclude photometric measurements for which no uncertainties are listed. If a quoted uncertainty is less than 0.01 mag, then we inflate the uncertainty to 0.01 mag to be conservative. We thus have an initial catalog of 2,539,914 stars with at least one flux measurement.

2.2. Literature Spectroscopic Parameters

We also queried VizieR for spectroscopically determined effective temperatures T_{eff} and metallicities to use as priors in our analysis. We began by searching for matches from the first LAMOST data release catalog (Luo et al. 2015), choosing the source with the closest match within $0.1'$. If no LAMOST match was found, we then searched the fourth RAVE data release catalog (Kordopatis et al. 2013). If a given RAVE match had multiple sets of spectroscopic parameters, then we adopted the parameters with the largest uncertainties (to avoid over-constraining our fits with possibly unrealistically small catalog uncertainties). If no RAVE match was found, we then searched the Apache Point Observatory Galactic Evolution Experiment (APOGEE) 13th data release (Blanton et al. 2017) from the Sloan Digital Sky Survey (SDSS Collaboration et al. 2016), including the post-hoc correction¹ to effective temperatures when available, and use the initial pipeline effective temperature otherwise (Holtzman et al., in preparation). Finally, if no SDSS spectroscopic [Fe/H] was found, then we assume the star has the median [Fe/H] of the measured distribution of late-type, solar neighborhood stars from the Geneva-Copenhagen Survey (Casagrande et al. 2011), and an ‘uncertainty’ equal to the $1-\sigma$ dispersion in this distribution; specifically, we adopt a metallicity [Fe/H] = -0.05 and uncertainty $\sigma_{[\text{Fe}/\text{H}]} = 0.22$.

Of our initial 2,539,913 stars, 74,515 have LAMOST DR1 temperatures and metallicities; an additional 239,017 have RAVE DR4 temperatures and metallicities; an additional 24,029 have APOGEE temperatures and metallicities; and the remaining 2,202,352 do not have temperatures and metallicities from the aforementioned datasets. We do not exclude giants *a priori*, nor do we identify blends, binaries, or multiple stellar systems. Our methods of estimating the temperature and bolometric flux (presented below) were successful for 1,600,080 stars; we list the photometry and spectroscopic parameters we used in Table 4. For the remainder of our analyses, we will separately consider these four subgroups—those with spectroscopic T_{eff} from (1) LAMOST, (2) RAVE, (3) APOGEE, and (4) those without spectroscopic T_{eff} —where appropriate.

2.3. Gaia DR1 Parallaxes

¹ <http://www.sdss.org/dr13/irspec/parameters/>

We adopt the parallax measurements from *Gaia* (Gaia Collaboration 2016). We adopt the *Gaia* parallax, π , and its uncertainty as provided by the first *Gaia* data release (DR1)² (see Table 6). A total of 424,489 stars in our sample have parallaxes in the Tycho-Gaia Astrometric Solution (TGAS) sample.

We note that, at the time of this writing, the *Gaia* team reports that the DR1 π values have systematic errors that are ~ 0.2 mas on small scales and zero-point variations as large as ~ 0.3 mas on large spatial scales.³ Preliminary assessments suggest a global offset of ~ -0.25 mas⁴ for $\pi \gtrsim 1$ mas (Stassun & Torres 2016b), corroborating the *Gaia* claim, based on comparison to directly-measured distances to well-studied eclipsing binaries by Stassun & Torres (2016a), which itself is based on the sample of Torres et al. (2010). Gould et al. (2016) similarly claim a systematic uncertainty of 0.12mas. Casertano et al. (2017) used a large sample of Cepheids to show that there is likely little to no systematic error in the *Gaia* parallaxes for $\pi \lesssim 1$ mas, but find evidence for an offset at larger π consistent with Stassun & Torres (2016b).

Thus the available evidence suggests that any systematic errors in the *Gaia* parallaxes are likely to be small. Therefore, for the purposes of this work, we simply use and propagate the reported *random* uncertainties on π only, emphasizing that (a) the fundamental F_{bol} and Θ measurements that we report are independent of π , and (b) additional (or different) choices of statistical and systematic uncertainties in π may be applied to our F_{bol} and Θ measurements following the methodology, equations, and error propagation coefficients supplied below.

Table 1. Stellar Sample Overview

Description	Spectroscopic	No Spectroscopic	Total
	Priors	Priors	
Stars in initial sample	337,561	2,202,353	2,539,914
Stars with iterative IRFM parameters	293,412	1,306,668	1,600,080
Stars with TGAS solutions	212,025	1,049,641	1,261,666
Stars with $\leq 10\%$ parallaxes	64,960	290,542	355,502

3. METHOD

The basic precepts for the methodology used here are from Stassun & Torres (2016a) and Stassun et al. (2016). Briefly, to calculate the radius of each star, we calculate its distance d from its *Gaia* parallax. The radius is then given by the equation $R_* = (\theta d)/2$, where

$$\theta \equiv 2 \left(\frac{F_{\text{bol}}}{\sigma T_{\text{eff}}^4} \right)^{1/2}. \quad (1)$$

² Accessed on 14 September 2016.

³ See <http://www.cosmos.esa.int/web/gaia/drl>

⁴ Where the negative sign indicates that the *Gaia* parallaxes are underestimated.

We then calculate the uncertainty on the radius as

$$\frac{\sigma_{R_*}}{R_*} = \sqrt{\left(\frac{\sigma_d}{d} \right)^2 + \left(\frac{\sigma_\theta}{\theta} \right)^2}, \quad (2)$$

where

$$\left(\frac{\sigma_\theta}{\theta} \right)^2 = \frac{1}{4} \left(\frac{\sigma_{F_{\text{bol}}}}{F_{\text{bol}}} \right)^2 + 4 \left(\frac{\sigma_{T_{\text{eff}}}}{T_{\text{eff}}} \right)^2 - 2\rho \left(\frac{\sigma_{T_{\text{eff}}}}{T_{\text{eff}}} \frac{\sigma_{F_{\text{bol}}}}{F_{\text{bol}}} \right) \quad (3)$$

and ρ is Pearson's correlation coefficient between T_{eff} and F_{bol} .

Thus, in the following subsections, we detail our procedures for measuring T_{eff} and F_{bol} for the stars in our study sample.

We do require some modifications in procedure compared to Stassun & Torres (2016a); Stassun et al. (2016) due to the very large size of our sample. In particular, rather than perform full broadband SED fits for all 2,539,913 stars for which we have photometry, we use empirical color- T_{eff} and color- F_{bol} relations, and perform full broadband SED fits for a subset of the stars in order to assess the reliability of the empirical relations.

We adopt this approach in this paper primarily out of practicality and convenience. The very large number of stars in our sample with available photometry makes full SED fitting very time consuming. Furthermore, we believe that the DR1 parallaxes are sufficiently imprecise that they do not warrant the more direct approach of fitting the SEDs, despite the deficiencies we encounter using the empirical color- T_{eff} and color- F_{bol} relations, as described below. Furthermore, the *Gaia* spectrophotometry, which will be released at a later date, will allow for much stronger constraints on the SEDs of the target stars. Therefore, in a future paper, we plan to perform full SED fits to all available photometry, including *Gaia* spectrophotometry, for all stars with sufficiently precise *Gaia* parallaxes.

In addition, we determine ρ in the equations above for each of our four subsamples separately. We note that these equations for the uncertainties on R_* and θ fundamentally assume that the mathematical relations between the inferred quantities and the observables are linear. In fact, this is not true in most cases, which implies that these relations are only accurate when the uncertainty in the measured quantity is small compared to the absolute value of the quantity itself. This can be particularly problematic in the case of the measured parallax $\pi \propto d^{-1}$, which is often measured to precision that is comparable to the value of π itself. Using parallaxes with uncertainties comparable to their magnitudes is also complicated by Lutz-Kelker bias (Lutz & Kelker 1973). In order to avoid these complications, we only include stars with $\sigma_\pi/\pi \lesssim 10\%$.

3.1. Stellar Parameters

3.1.1. Effective Temperature

In principle, if we were only interested in inferring the angular diameters of our sample of stars (and from these diameters inferring radii using the *Gaia* parallaxes), we could simply adopt empirically-calibrated color-angular diameter relations (e.g., Boyajian et al. 2014). However, we chose to

instead derive T_{eff} and F_{bol} individually from separate empirical color- T_{eff} and color- F_{bol} relations, for two reasons. First, we can compare our inferred estimates of T_{eff} with spectroscopic measurements, thus validating our inferred values and allowing us to use the spectroscopic T_{eff} as constraints. Second, we do not know the extinction to the stars in our sample *a priori*. A significant extinction would bias the broadband photometry we use to infer the angular diameters, thereby leading to a bias in the angular diameters and radii. We must therefore estimate the extinction as well⁵.

In order to infer T_{eff} , we apply the Casagrande et al. (2010) infrared flux method (IRFM) relations, to obtain effective temperatures for the Tycho-2 stars. As noted above, to do so, however, it is first necessary to de-redden the photometric measurements. Since we do not know the extinction A_V *a priori*, we estimate the extinction and the effective temperature as follows:

1. We step through $N_i = A_{V,\text{max}}/\Delta A_V$ extinction values $A_{V,i}$ in increments of $\Delta A_V = 0.01$ over the range $A_V \in \{0, A_{V,\text{max}}\}$, where $A_{V,\text{max}} \equiv E_{B-V}R_V$ is the maximum line-of-sight total extinction, estimated from is the maximum line-of-sight color excess (selective extinction) E_{B-V} determined from the Schlegel et al. (1998) dust maps, and adopting $R_V = 3.1$ for the ratio of total to selective extinction. We note that, despite the caution indicated by Schlegel et al. (1998), we adopt their maximum color excess even for stars within 10° of the Galactic plane. We will provide qualitative tests of the validity of our inferred extinctions for stars in this region of the sky in a later section.
2. At each value of $A_{V,i}$, we de-redden the photometric magnitudes using the (Cardelli et al. 1989) extinction law. We then calculate $T_{\text{eff},j}$ from each of $j = 0, 1, \dots, N_j$ applicable Casagrande et al. (2010) empirical relations for which the de-reddened color and the metallicity are within the applicable ranges. The uncertainty $\sigma_{T_{\text{eff},j}}$ on the $T_{\text{eff},j}$ derived from each relation is calculated as the square-root of the quadrature sum of the standard deviation about the empirical relation listed in Table 4 of Casagrande et al. (2010) and the (linearly) propagated uncertainty due to the (assumed to be independent) errors on $[\text{Fe}/\text{H}]$ and the photometric measurements. If no empirical relations apply – e.g. because all de-reddened colors lie outside the suitable ranges for all IRFM relations – then we skip to the next $A_{V,i}$.
3. We calculate the weighted mean $T_{\text{eff,mean},i}$ for each $A_{V,i}$ from all N_j applied relations, where we weight each $T_{\text{eff},j}$ by the square of the uncertainty in each relation $\sigma_{T_{\text{eff},j}}$. We then reject $T_{\text{eff},j}$ if $T_{\text{eff},j} - T_{\text{eff,mean},i} > 3\sigma_{T_{\text{eff},j}}$. We then re-calculate the weighted mean $T_{\text{eff,mean},i}$ and

iterate until no outliers remain or until only one relation remains.

4. We calculate a "merit function" $\chi_{\text{IRFM}}^2 \equiv \sum_{j=0}^{N_j} (T_{\text{eff},j} - T_{\text{eff,mean},i})^2 / \sigma_{T_{\text{eff},j}}^2$, which essentially quantifies how well values all the N_j inferred values of $T_{\text{eff},j}$ are consistent with a constant value of T_{eff} , given their respective uncertainties $\sigma_{T_{\text{eff},j}}$ and the assumed value of $A_{V,i}$.
5. We add a penalty term $\chi_{\text{spec}}^2 \equiv (T_{\text{eff,mean},i} - T_{\text{eff,spec}})^2 / \sigma_{T_{\text{eff,spec}}}^2$ if a spectroscopic T_{eff} exists. If $\chi^2 = 0$ because there is no spectroscopic effective temperature for this star and only one calibration relation applies, then we skip to the next $A_{V,i}$.
6. We select the value $A_{V,i}$ and the error-weighted mean $T_{\text{eff,mean},i}$ corresponding to the minimum $\chi^2 \equiv \chi_{\text{IRFM}}^2 + \chi_{\text{spec}}^2$. If no merit function was calculated for any value of $A_{V,i}$, then we have insufficient information to inform our choice of effective temperature; therefore, we drop this star from the sample and move onto the next star.
7. We re-scale the uncertainty on $T_{\text{eff,mean},i}$ such that $\chi_\nu^2 = 1$ for the minimum χ^2 , where the χ_ν^2 is reduced χ^2 with ν degrees of freedom. Explicitly, the scale factor is

$$\sqrt{\frac{1}{N_j + 1} \left[(T_{\text{eff,mean},i} - T_{\text{eff,spec}})^2 + \sum_{j=0}^{N_j} (T_{\text{eff},j} - T_{\text{eff,mean},i})^2 \right]} \quad (4)$$

if there is a spectroscopic T_{eff} and

$$\sqrt{\sigma_{T_{\text{eff,mean}}} \equiv \frac{1}{N_j} \sum_{j=0}^{N_j} [(T_{\text{eff},j} - T_{\text{eff,mean},i})^2]} \quad (5)$$

if not. We re-calculate $T_{\text{eff,mean},i}$ using these rescaled uncertainties.

8. We then estimate the uncertainty on the extinction by taking the range of extinctions corresponding to $\Delta\chi^2 = 1$, using this scaled uncertainty. If no extinctions lie within this range, then we adopt our stepsize, $\Delta A_V = 0.01$, as the uncertainty.

If no IRFM relations were applied for any extinction, we drop the star from the sample. Additionally, for the stars without spectroscopic temperatures, if there exists an extinction for which only one IRFM relation applies, then the merit function $\chi^2 = 0$ by definition for that extinction. In these cases, we infer that we do not have enough information to determine both extinction and T_{eff} , and so we also drop such stars from our sample.

3.1.2. Bolometric Flux

We estimate the unextinguished bolometric flux F_{bol} as follows:

1. We de-redden the magnitudes with the extinctions obtained in Section 3.1.1 and apply all $N_{F_{\text{bol}}}$ applicable Casagrande et al. (2010) bolometric flux relations.

⁵ We note, as is well known, that color-angular diameter relations are fairly insensitive to extinction. However, they are not *completely* insensitive to extinction, and some color indices are more sensitive to extinction than others. Furthermore, a significant fraction of our sample are giant stars, which may be quite far from the Sun, and for which the extinction may be significant, particularly near the Galactic plane.

2. For each relation, we calculate the mean error-weighted bolometric flux, F_{bol} , and the weighted uncertainty on the flux, $\sigma_{F_{\text{bol}}}$, where the weights are the quadrature sums of the scatter about each relation as cited by [Casagrande et al. \(2010\)](#) and the (linearly) propagated uncertainties due to the uncertainties on the magnitudes, extinction, and [Fe/H], assuming all uncertainties are independent. As with the effective temperature procedure, if no IRFM relations were applicable – e.g. because the de-reddened color lies outside the ranges of all relations – we drop the star from our sample.
3. We calculate $\chi_{F_{\text{bol}}}^2 \equiv \sum_{j=0}^{N_{F_{\text{bol}}}} (F_{\text{bol},j} - F_{\text{bol,mean}})^2 / \sigma_{F_{\text{bol},j}}^2$ and scale the uncertainties by a constant factor such that $\chi_{\nu, F_{\text{bol}}}^2 = 1$, where $\nu = N_{F_{\text{bol}}}$. We then re-calculate $F_{\text{bol,mean}}$ and $\sigma_{F_{\text{bol,mean}}}$ using these rescaled uncertainties.

3.2. Validating T_{eff} and F_{bol} Determined via the Iterative IRFM Technique

Before we apply the *Gaia* parallaxes to infer radii for the $\sim 356,000$ stars in our final sample, we first validate our technique for inferring the T_{eff} and F_{bol} for the over 1.6 million stars that remain in our sample after applying the IRFM to infer T_{eff} and F_{bol} .

3.2.1. Extinctions

As one way of validating the results of our iterative procedure outlined in Section 3, we check that our method prefers reasonable extinction values. First, we examine the distribution of extinctions across Galactic latitude b ; most of the highly extinguished stars should lie in the Galactic disk – roughly $|b| < 10^\circ$ – where there is more dust along a typical line of sight. Figure 1 shows these distributions for the four subsamples; indeed, the most highly extinguished stars are those in the disk.

3.2.2. Comparison to Spectroscopic Effective Temperatures

Figure 2 show the IRFM-derived effective temperatures versus the spectroscopic values for the resulting sample of 64,345 LAMOST stars, 214,707 RAVE stars, and 14,360 APOGEE stars.

This excludes stars with reduced $\chi_\nu^2 > 100$, which effectively removes stars for which the IRFM temperatures and spectroscopic temperatures differ by $\mathcal{O}(10^3 \text{ K})$. Notably, these include many giants, for which the IRFM relations were not calibrated. The IRFM effective temperatures are positively correlated with the spectroscopic temperatures; stars with discrepant temperatures tend to have higher χ^2 values, while the IRFM temperatures for stars with lower χ^2 values tend to agree with the spectroscopic values. Moreover, our iterative IRFM technique appears to systematically underestimate the effective temperatures for stars with spectroscopic temperatures above 7,000 K.

Figure 3 shows our effective temperature distributions inferred using the IRFM for the stars in our sample that also have spectroscopically-measured effective temperatures. In the RAVE sample, [Kordopatis et al. \(2013\)](#) use a grid of synthetic stellar spectra to derive the stellar parameters; hence,

the peaks in the histogram correspond to the T_{eff} grid points and are separated by the grid resolution of 250 K. As shown in Figure 2, the iterative IRFM technique infers an excess of stars with $T_{\text{eff}} > 7,000 \text{ K}$ relative to the spectroscopically-determined temperature distributions for the stars with LAMOST, RAVE, and APOGEE spectra. These stars typically have very few photometric measurements with which to infer T_{eff} , F_{bol} , and A_V , and our inferences about their properties are thus highly suspect. Therefore, we urge the reader to use extreme caution when applying our results for stars hotter than about 7,000 K.

As discussed below, the uncertainty on the *Gaia* parallax distances begin to dominate the radius error budget beyond $\sim 100 \text{ pc}$ (see also [Stassun et al. 2016](#)). The uncertainty in radius due to the error on the projected end-of-mission *Gaia* parallax should be greatly improved; for example, at 100 pc, the parallax signal is 10 milliarcseconds, so a projected 10 microarcsecond uncertainty translates to a 0.1% uncertainty on the radius.

3.2.3. Effect of Metallicity on IRFM Temperatures and Fluxes

As mentioned in Section 2.1, for the stars without measured metallicities, we adopt a metallicity and uncertainty equal to the median [Fe/H] and dispersion from the Geneva-Copenhagen Survey of late-type, solar neighborhood stars ([Casagrande et al. 2011](#)), as described in Section 3. To determine what effect our choice of metallicity has on the recovered effective temperatures and bolometric fluxes, we repeat our method for the subset of stars with spectroscopic parameters, this time using the Geneva-Copenhagen median and 1σ metallicity instead of the LAMOST metallicities. As Figure 4 illustrates, our decision to use the median and dispersion of the Geneva-Copenhagen survey as a proxy for the metallicity of stars without directly-measured metallicities has a negligible effect on the temperature and bolometric flux we infer for these stars from our iterative IRFM procedure.

3.2.4. Comparison to Full Broad-band Spectral Energy Distributions

Nominally, the IRFM relations of [Casagrande et al. \(2010\)](#) are parameterizations of stellar spectral energy distributions (SEDs). As another check on our effective temperatures, bolometric fluxes, and angular diameters, we generate SEDs for 132 stars in common between our sample and the [Casagrande et al. \(2010\)](#) sample. We use Kurucz model atmospheres ([Kurucz 2013](#)) to fit SEDs to Tycho-2, [Mermilliod \(2006\)](#), [Paunzen \(2015\)](#), 2MASS, GALEX NUV ([Bianchi et al. 2011](#)) and WISE ([Cutri & et al. 2014](#)) photometry when available. As before, we adopt the listed measurement uncertainties unless these uncertainties are smaller than 0.01 mag (or 0.1 mag for the GALEX NUV and WISE4 bands); in these cases, we adopt 0.01 mag (0.1 mag) as the measurement uncertainties. In addition, to account for an artifact in the Kurucz atmospheres at $10\mu\text{m}$, we artificially inflate the WISE3 uncertainty to 0.3 mag unless the reported uncertainty was already larger than 0.3 mag. Additionally, we iteratively clip 5σ outlier measurements.

We sample the effective temperature at the [Casagrande et al. \(2010\)](#) listed value as well as $\pm 1\sigma$. We fix $\log g_*$ and

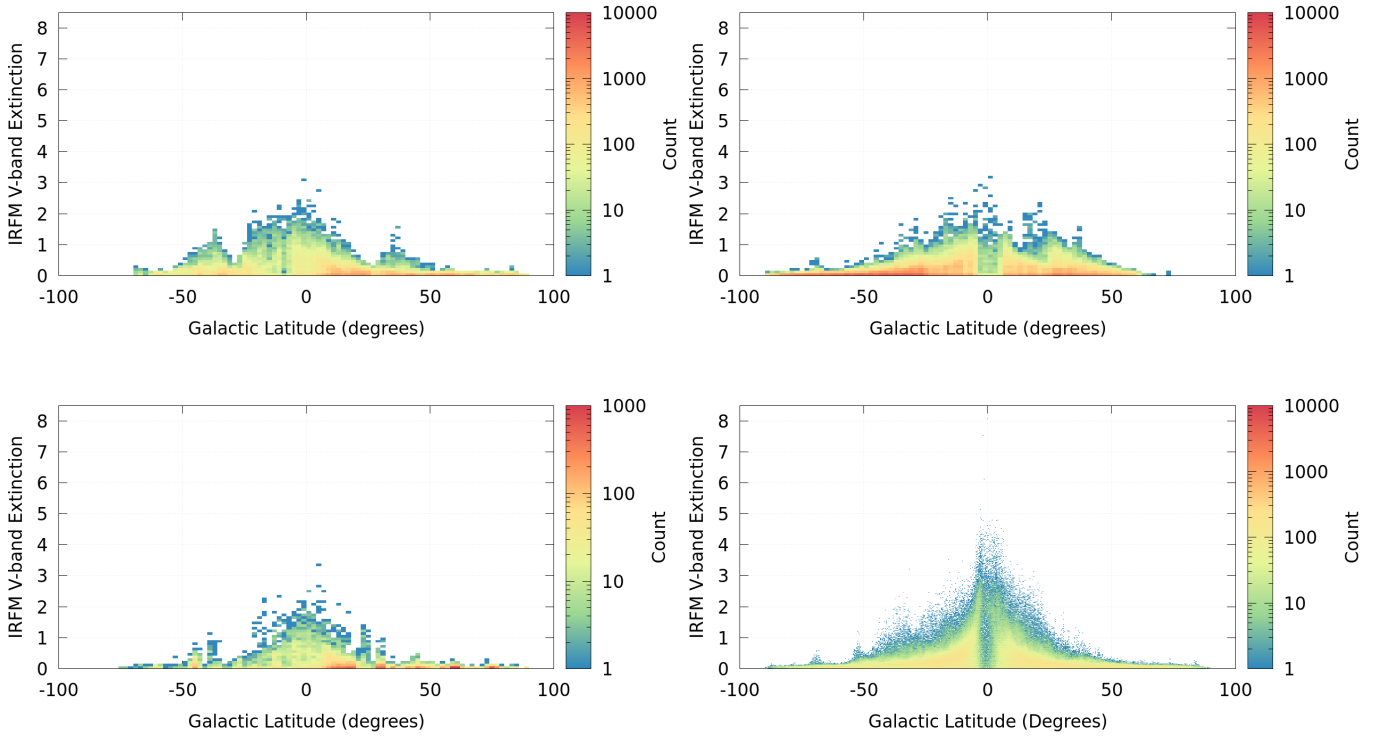


Figure 1. Best-fit extinction values A_V , as a function of Galactic latitude b for the stars in the LAMOST (*top-left*), RAVE (*top-right*), APOGEE (*bottom-left*), and non-spectroscopic (*bottom-right*) samples.

[Fe/H] to the Casagrande et al. (2010) values, rounded to the nearest values for which a Kurucz model atmosphere exists. We sample ten extinctions from $A_V = 0$ to the maximum line-of-sight extinction from the Schlegel et al. (1998) dust maps. We show our SEDs in Appendix A. Figures 5, 6, 7, 8, 9 compare the iterative IRFM extinctions, effective temperatures, bolometric fluxes, and angular diameters, respectively, to those from the SEDs. We find generally good agreement between the two methods. We note that, for the majority of stars, the SED and iterative IRFM extinctions agree quite well – as seen in the bottom two panels of Figure 6 – though we overestimate the extinctions relative to the SED values for a few systems in the tail of the aforementioned histogram. Correspondingly, we overestimate the effective temperatures and bolometric fluxes for these stars and underestimate the angular diameters relative to the model SEDs at the level of a few percent. We see no trend with unscaled reduced χ^2 . The model SED fits to the photometry are shown in Figure A1 and can be seen to fit the data well overall.

4. RESULTS

4.1. Effective Temperatures, Bolometric Fluxes, and Angular Diameters

For each subsample, Tables 2 and 3 list the number of stars and median values plus 68% confidence interval values for the unscaled χ^2_ν and the fractional precision on the effective temperature, bolometric flux, and angular diameter for the full sample of stars and the subset of stars with radii, respectively. We note that the larger median T_{eff} uncertainties for

the spectroscopic sample, which lead to larger median angular diameter and radius uncertainties, are the result of including the nonzero χ^2 penalty when re-scaling the uncertainties. This suggests that the uncertainties are likely underestimated.

We attempt to inflate these lower uncertainties by repeating the iterative IRFM method on the stars with spectroscopic parameters without applying the T_{eff} prior. We then bin the spectroscopic stars according to the IRFM T_{eff} without the prior, in bins of 100K. In each bin, we calculate the median A_V , T_{eff} and F_{bol} uncertainties with the prior and calculate the ratio of these median uncertainties to the median uncertainties without the prior. Finally, we bin up the non-spectroscopic stars in the same T_{eff} bins and, for each star in each bin, we multiply the A_V , T_{eff} , and F_{bol} uncertainties by these ratios. The scaled uncertainties on T_{eff} and F_{bol} as well as the propagated uncertainties on the angular diameter and linear radius are given as the last columns in Tables 2 and 3. We emphasize again that we *post-hoc* inflate the parameter uncertainties for the stars without spectroscopic priors to try to compensate for our method’s underestimation of these uncertainties. The full SED fits that we will perform in future work will elucidate the accuracy of these uncertainties.

Figure 10 shows the χ^2 distributions, while Figures 11, 12, and 13 show the fractional effective temperature precision, fractional bolometric flux precision, and fractional angular diameter distributions for the four subsamples, respectively.

We emphasize that these bolometric fluxes and angular diameters are fundamental, empirical products of this study

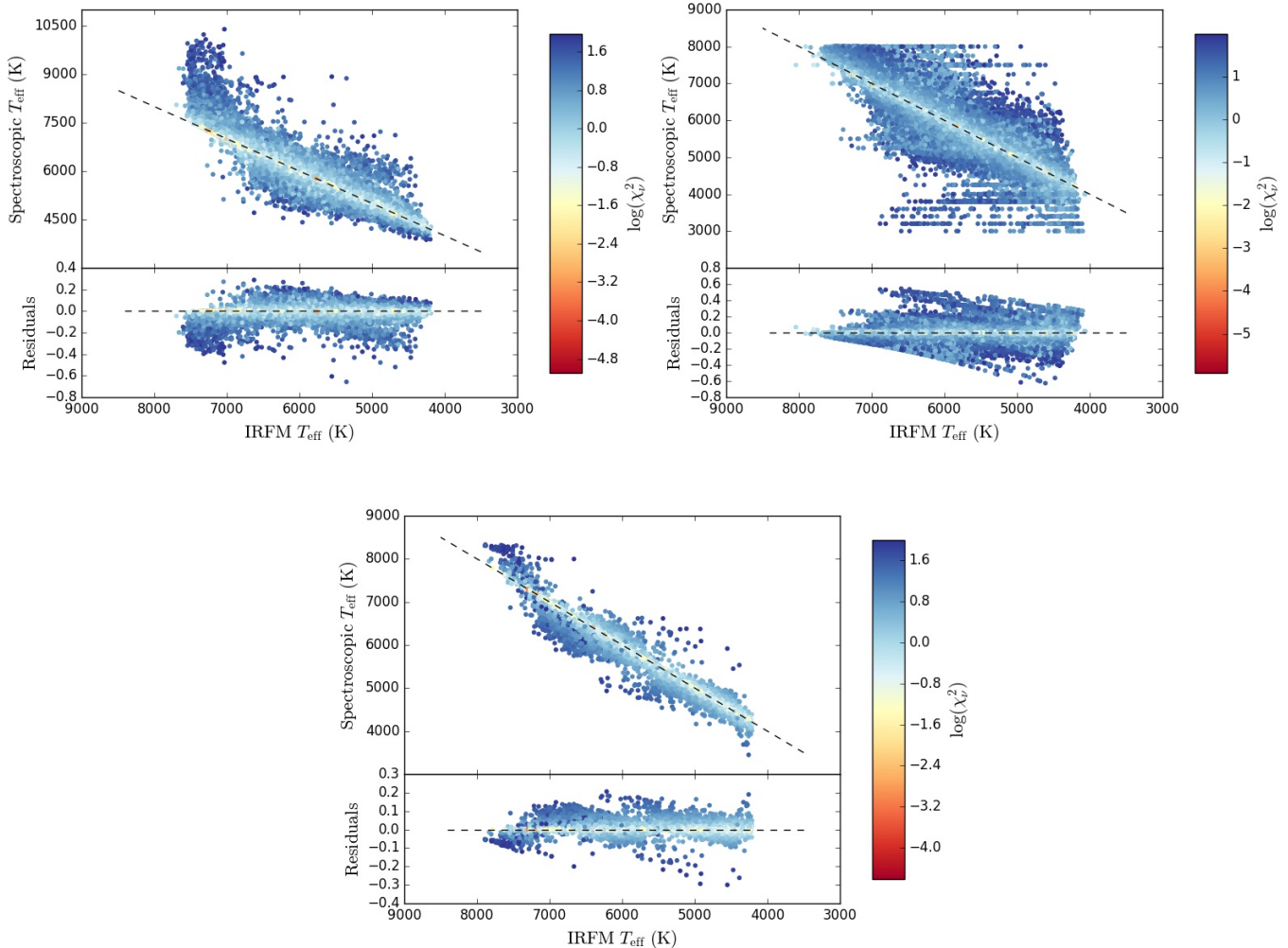


Figure 2. Spectroscopic versus best-fit effective temperatures T_{eff} (top sub-panels) and the fractional deviations (bottom sub-panels) for the stars in our LAMOST (*top-left*), RAVE (*top-right*), and APOGEE (*bottom*) samples. The colors denote the unscaled $\log \chi^2_{\nu}$.

that can be utilized to determine linear radii and other quantities as the *Gaia* parallaxes improve with upcoming data releases. We present the determined extinctions, temperatures, bolometric fluxes, and angular diameters for these stars in Table 5.

4.2. Radii

We queried the *Gaia* DR1 archive for parallaxes and proper motions from the Tycho-Gaia Astrometric Solution for our $\sim 1,600,080$ stars. Of this sample, 1,289,988 stars have *Gaia* parallaxes and proper motions. 1,280,289 of these stars have non-negative parallaxes; we suspect that the negative parallaxes quoted for some stars are due to orbital motion in binary and multiple stellar systems, as *Gaia* DR1 treats all sources as single stars. Of these, 1,153,804 of these stars have fractional parallax uncertainties better than 50%, while 355,502 have fractional parallax uncertainties better than 10%.

We restrict ourselves to stars with parallax uncertainties $\lesssim 10\%$ not least of all because stars with worse parallax precision are more subject to Lutz-Kelker bias (Lutz & Kelker

1973): specifically, the observed parallax systematically exceeds the true parallax by an amount that increases with increasing fractional parallax uncertainty. The effect of our precision cut can be seen in Figure 14 as a steep decline in the number of stars with fractional radius uncertainties larger than 10%.

We calculate the distances and radii for these stars. We list the median and 68% confidence interval values for the reduced χ^2 and fractional effective temperature, bolometric flux, angular diameter, and radius uncertainties in Table 3, and we list the values themselves in Table 6. We achieve $< 10\%$ median uncertainties on the stellar radius in all four subsamples. Following Equations 1 and 2 and as shown in Figure 15, we see that our quoted effective temperature uncertainties of a couple percent – along with the several-percent uncertainties on the parallaxes – dominate the radius error budget.

In both panels of Figure 15, we see that the radius uncertainty is fundamentally bounded by the increasing parallax uncertainty at greater distances. If *Gaia* achieves the

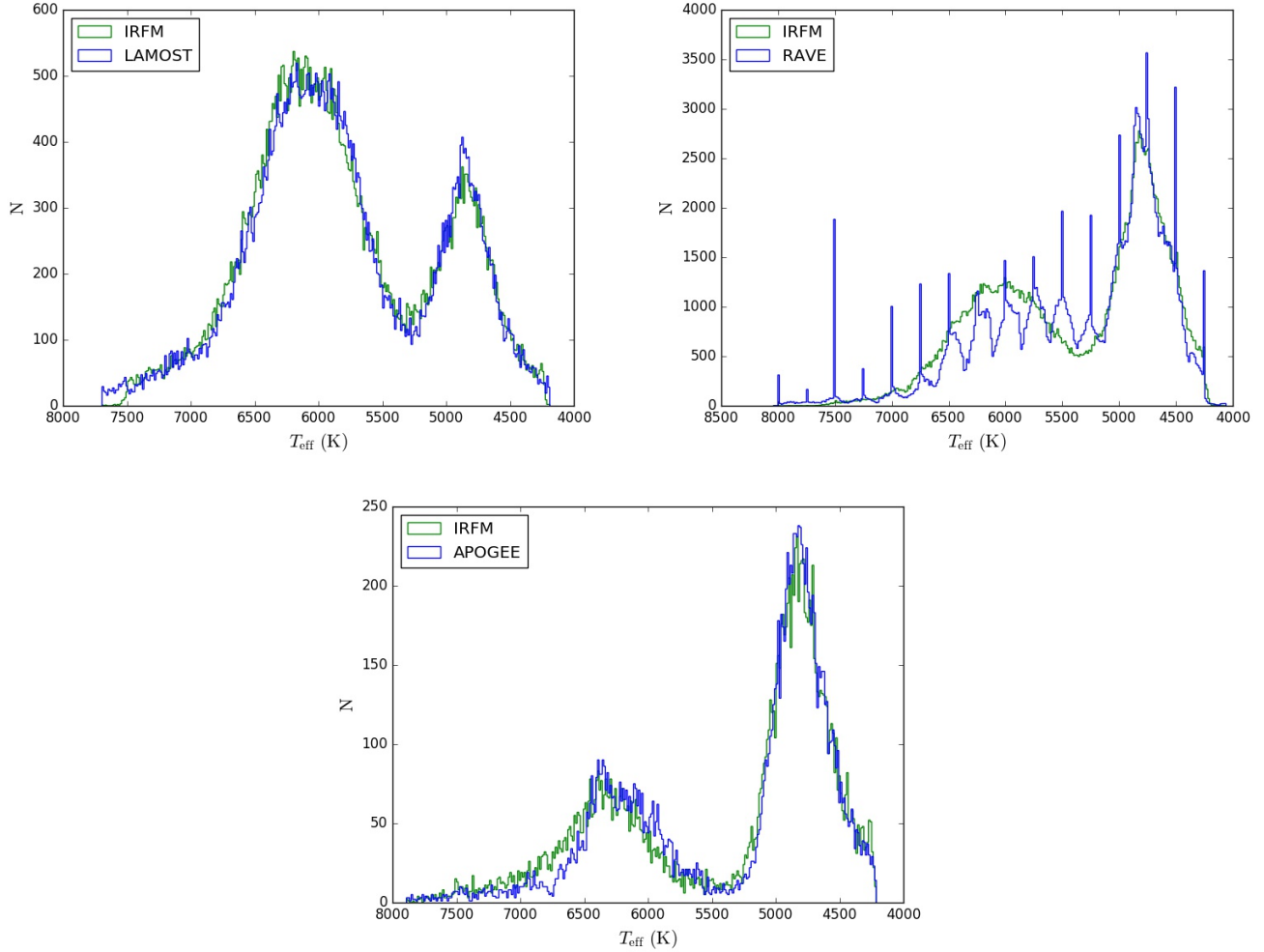


Figure 3. Spectroscopic versus best-fit effective temperatures T_{eff} for the stars in our LAMOST (*top-left*), RAVE (*top-right*), and APOGEE (*bottom*) samples. In all three cases, our iterative IRFM procedure appears to be slightly biased towards hotter effective temperatures. The peaks in the RAVE histogram correspond to the grid resolution of synthetic spectra used by [Kordopatis et al. \(2013\)](#) in the stellar parameter pipeline pipeline: the grid steps in $\Delta T_{\text{eff}} = 250\text{K}$ increments.

predicted end-of-mission uncertainty of $\sim 20 \mu\text{s}$ for bright stars, then obtaining sufficiently precise (and, given the required precision, accurate) effective temperatures becomes the paramount challenge to obtaining precise radii, particularly at the 3–5% level.

4.3. Empirical Hertzsprung-Russell Diagram

Figure 16 shows luminosity-temperature diagrams (‘theorists’ HR diagrams) for our stars. Dwarf, subgiant, and giant populations are coarsely identifiable by eye. The top panel, corresponding to the spectroscopic sample, also shows distinct groupings according to metallicity. Specifically, the metal-poor stars sit below the main sequence and to the left of the giant branch, as expected: metal-poor main-sequence stars tend to be slightly hotter and smaller than their metal-rich counterparts. The relative abundance of early-type and evolved stars versus late-type non-evolved stars is likely the result of Malmquist bias.

Table 2. Median Values of and 68% Confidence Intervals for 1,600,080 Tycho-2 Stars with Iterative-IRFM Temperatures, Fluxes, and Angular Diameters

Parameter	Value				
	LAMOST	RAVE	APOGEE	No Prior (Unscaled) (Scaled)	
Number of stars	64,345	214,707	14,360	1,306,668	1,306,668
Median Unscaled χ^2_{ν}	$0.42^{+1.21}_{-0.32}$	$0.64^{+1.94}_{-0.47}$	$0.49^{+2.04}_{-0.37}$	$0.25^{+0.60}_{-0.21}$	$0.25^{+0.60}_{-0.21}$
Median $\sigma_{T_{\text{eff}}}/T_{\text{eff}}$ (%)	$1.14^{+1.63}_{-0.67}$	$0.90^{+1.44}_{-0.52}$	$0.75^{+1.62}_{-0.44}$	$0.59^{+0.83}_{-0.37}$	$1.05^{+1.61}_{-0.68}$
Median $\sigma_{F_{\text{bol}}}/F_{\text{bol}}$ (%)	$2.69^{+4.83}_{-1.95}$	$1.77^{+2.87}_{-1.13}$	$1.64^{+2.99}_{-1.08}$	$2.07^{+4.31}_{-1.50}$	$1.86^{+3.94}_{-1.35}$
Median σ_{θ}/θ (%)	$3.19^{+3.91}_{-1.89}$	$2.28^{+3.14}_{-1.27}$	$2.04^{+3.69}_{-1.19}$	$1.88^{+2.57}_{-1.18}$	$2.69^{+3.63}_{-1.69}$

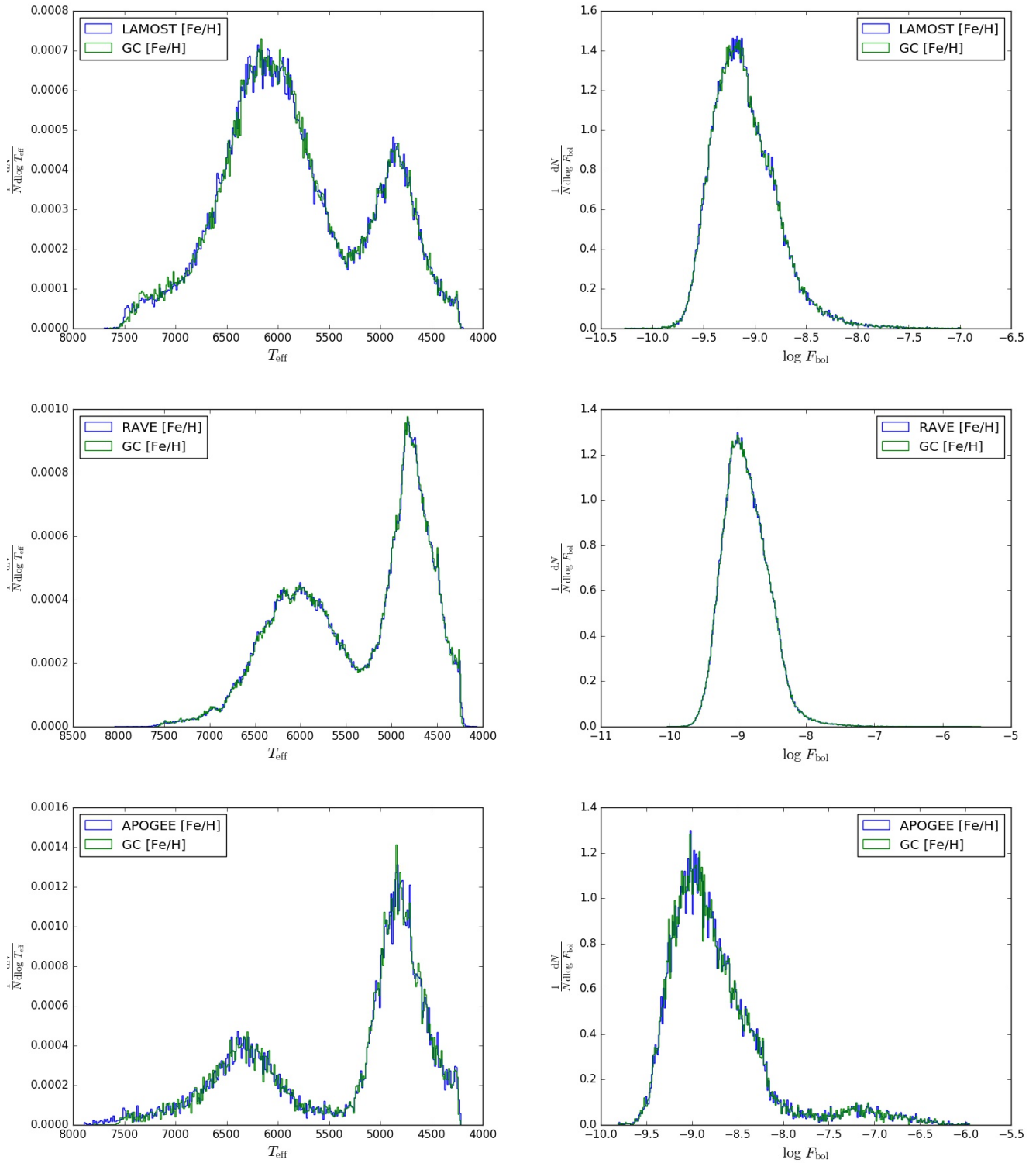


Figure 4. IRFM effective temperature (left) and bolometric flux (right) histograms using spectroscopically-determined metallicities of individual stars (blue) and assuming a metallicity and uncertainty for all stars equal to median and dispersion of the distribution of $[\text{Fe}/\text{H}]$ of stars from the Geneva-Copenhagen Survey (Casagrande et al. 2011) (green) for the LAMOST (top row), RAVE (middle row), and APOGEE (bottom row) stars. Overall, metallicity has a negligible effect on the recovered temperatures and fluxes.

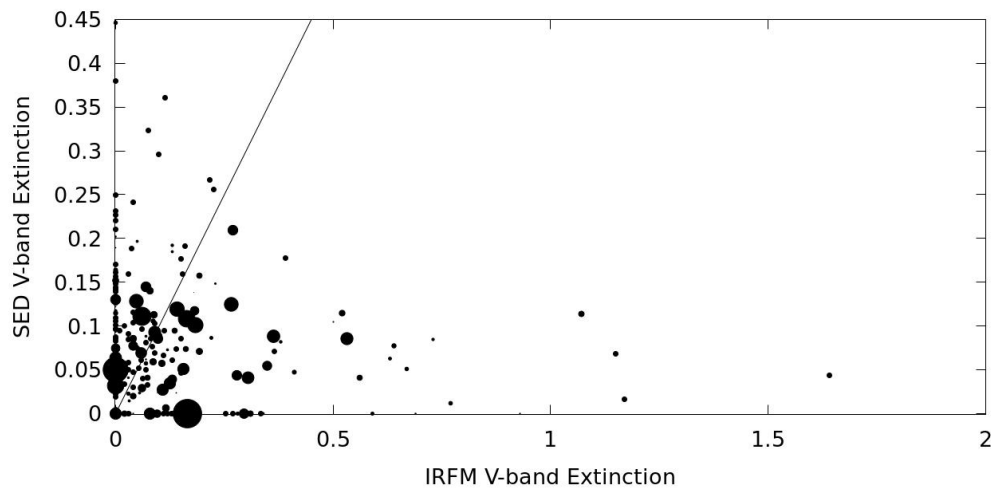


Figure 5. SED versus iterative IRFM extinction. The black line shows what would be perfect agreement between the two methods.

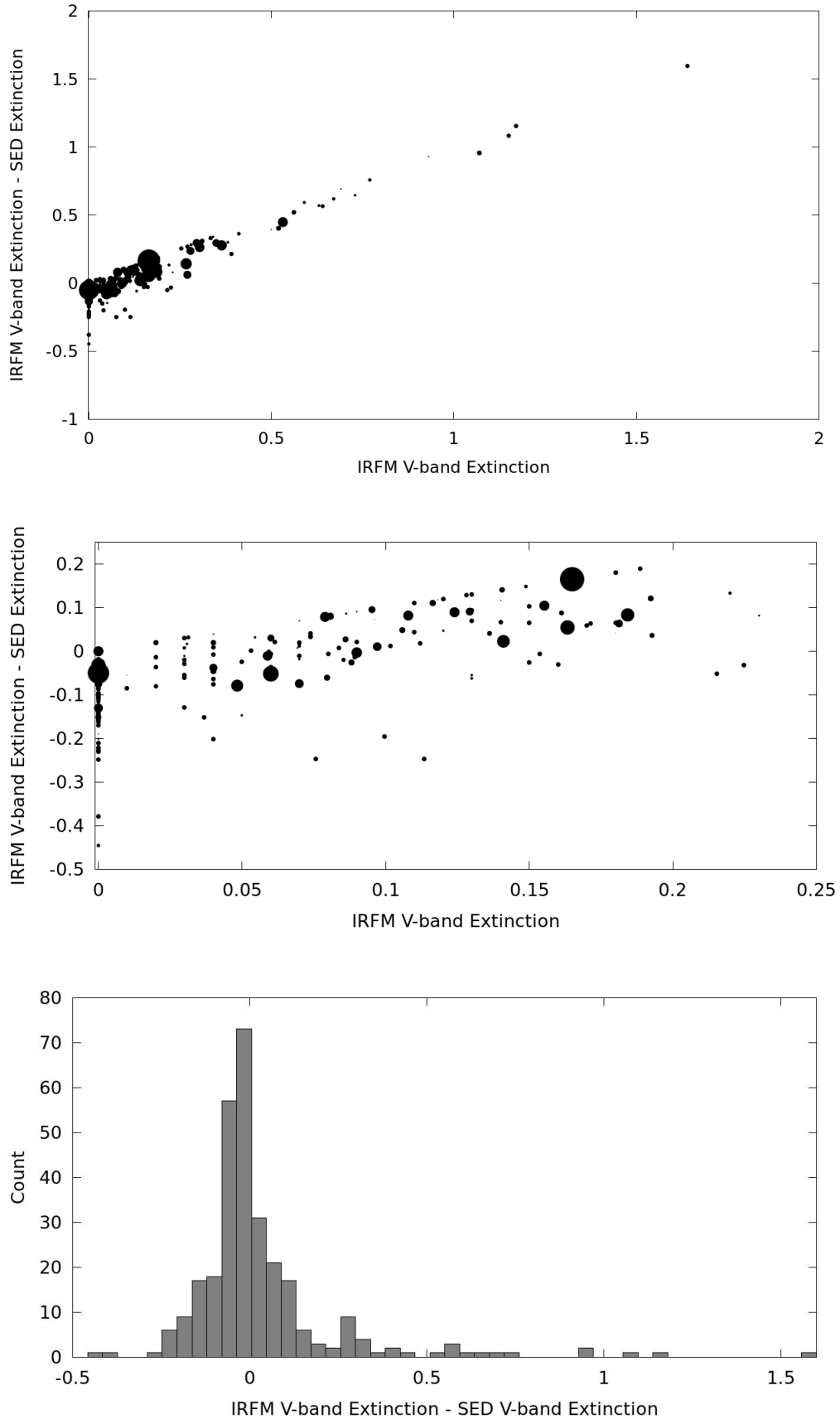


Figure 6. *Top:* Difference between IRFM and SED extinctions. In both panels, larger points denote higher χ^2_V values. The largest fractional deviations are for the lowest extinctions. *Middle:* Zoom-in of the top panel showing that the IRFM and SED extinctions agree reasonably well for the majority of stars in this comparison. *Bottom:* Histogram showing the absolute difference between the IRFM and SED extinctions. The median and standard deviation of the absolute differences between the IRFM and SED extinctions are, respectively, -4.5×10^{-3} and 2.2×10^{-1} .

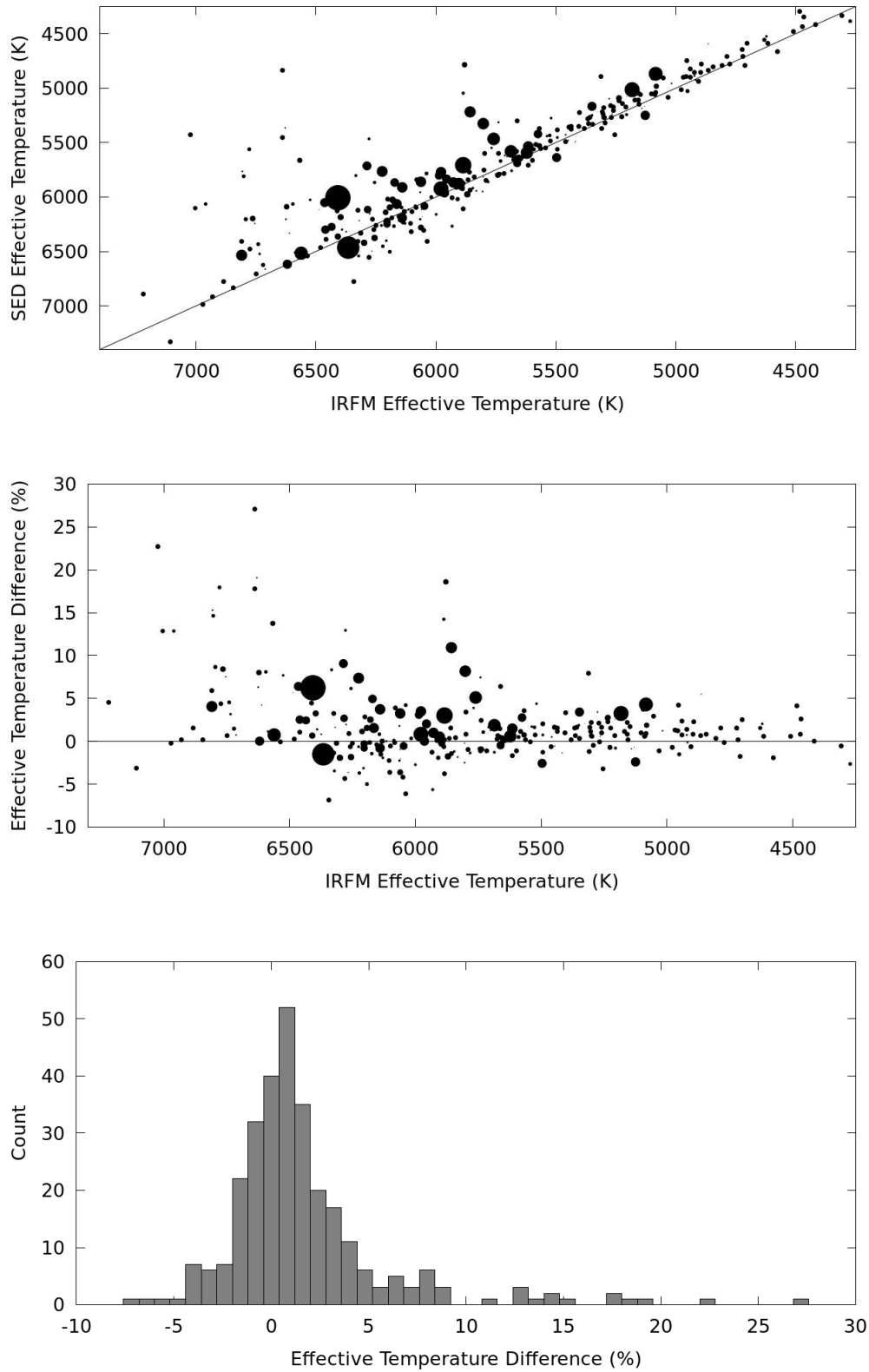


Figure 7. *Top:* SED versus iterative IRFM effective temperatures (right). The black line shows what would be perfect agreement between the two methods. *Middle:* Fractional difference between the IRFM and SED values relative to the IRFM values. In both panels, larger points denote higher χ^2_ν values. The median and standard deviation of the fractional differences are, respectively, 0.81% and 19%. *Bottom:* Histogram showing the absolute difference between the IRFM and SED effective temperatures.

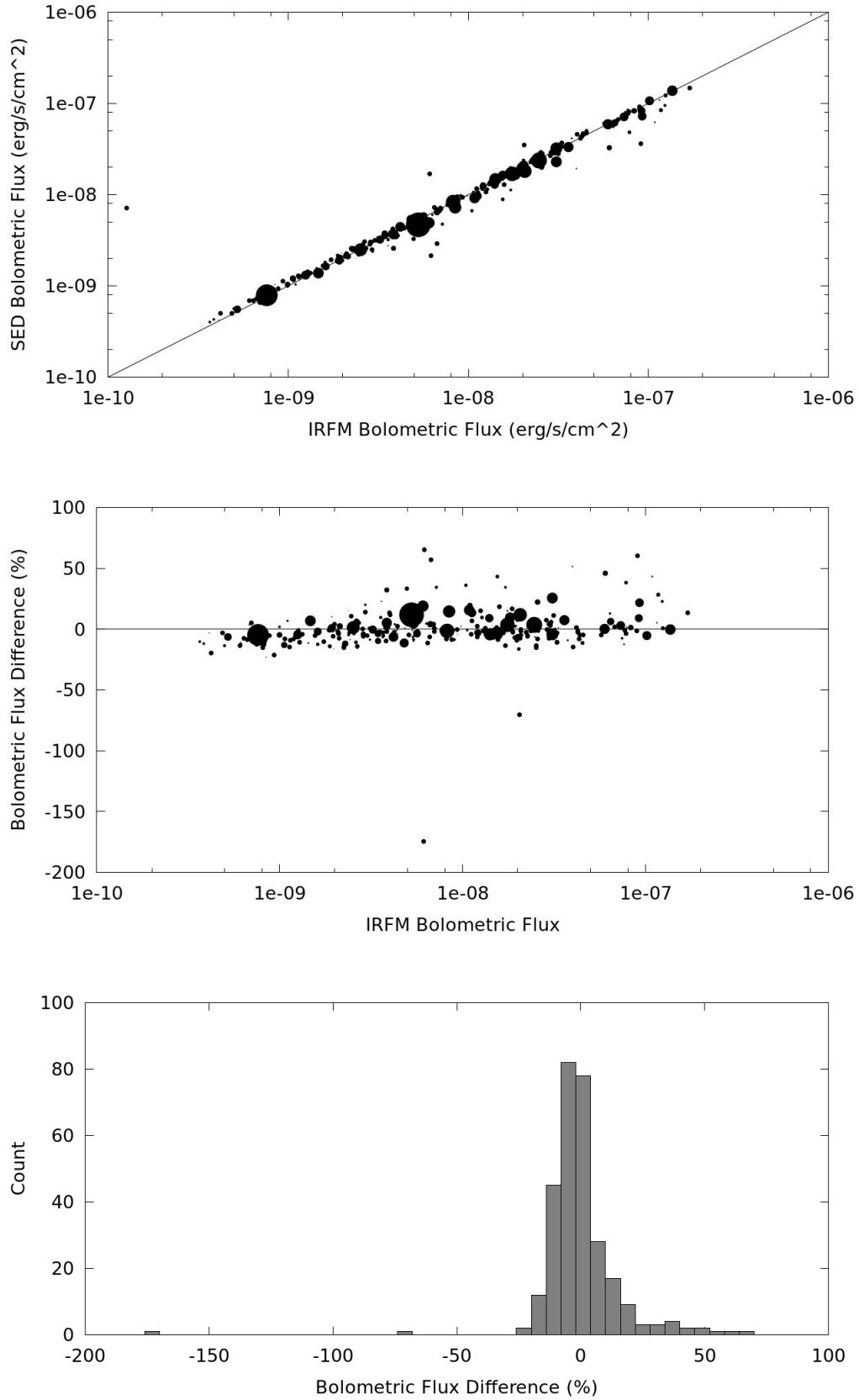


Figure 8. *Top:* SED versus iterative IRFM bolometric fluxes. The black line shows what would be perfect agreement between the two methods. *Middle:* Fractional difference between the IRFM and SED values relative to the IRFM values; negative values indicate smaller SED values. The median and standard deviation of the fractional differences are, respectively, -1.8% and 17%. *Bottom:* Histogram showing the absolute difference between the IRFM and SED bolometric fluxes.

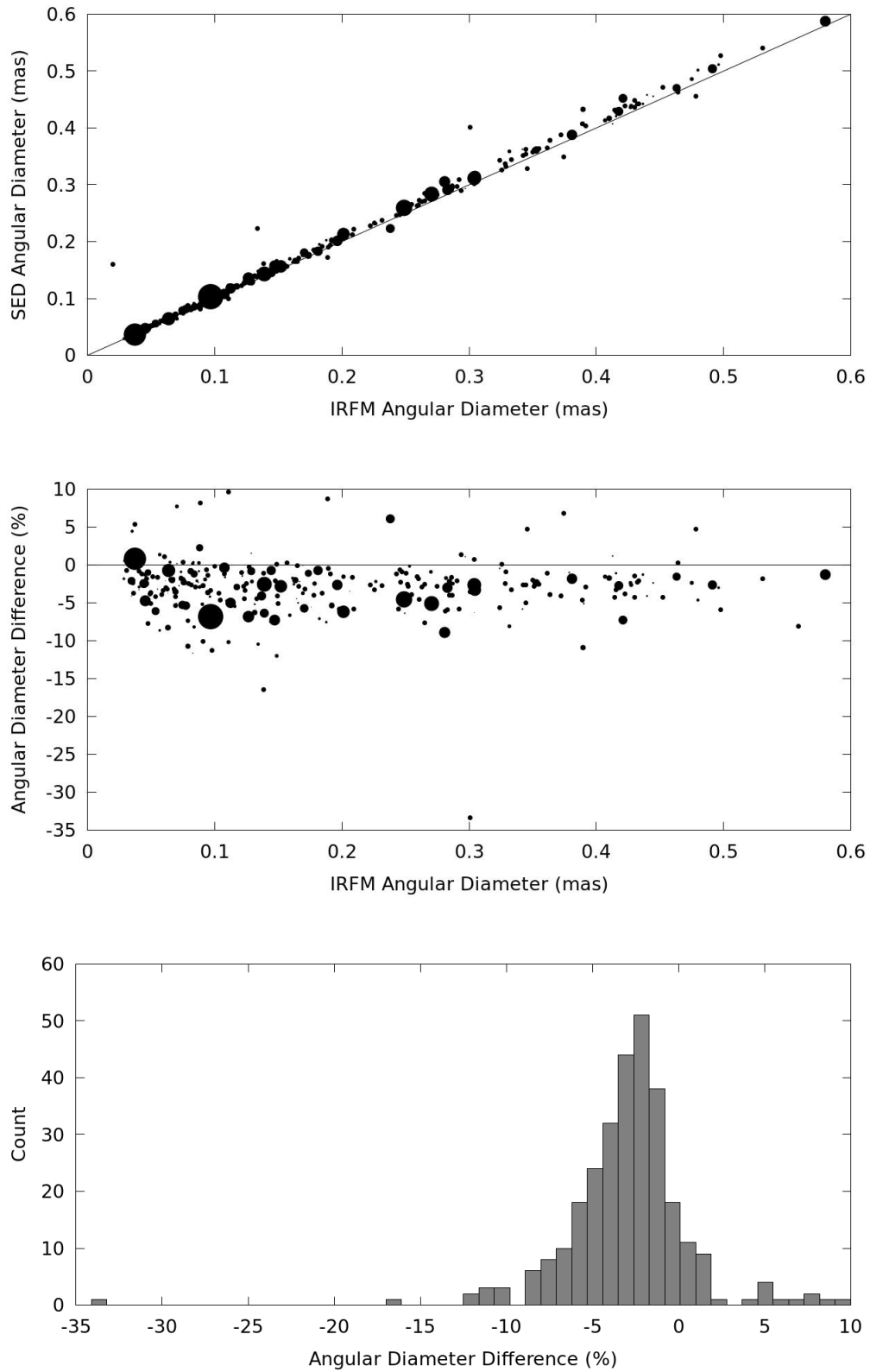


Figure 9. *Top:* SED versus iterative IRFM angular diameters. The black line shows what would be perfect agreement between the two methods. *Middle:* Fractional difference between the IRFM and SED values relative to the IRFM values. In both panels, larger points denote higher χ^2_ν values. The median and standard deviation of the fractional differences are, respectively, -2.7% and 3.6%. *Bottom:* Histogram showing the absolute difference between the IRFM and SED angular diameters.

Table 3. Median Values of and 68% Confidence Intervals for 355,502 Tycho-2 Stars with *Gaia* Astrometry

Parameter	Value				
	LAMOST	RAVE	APOGEE	No Prior (Unscaled)	(Scaled)
Number of stars	12,874	49,405	2,681	290,542	290,542
Median Unscaled χ^2_ν	0.38 ^{+0.97} _{-0.28}	1.05 ^{+2.72} _{-0.78}	0.72 ^{+2.63} _{-0.53}	0.28 ^{+0.59} _{-0.23}	0.28 ^{+0.59} _{-0.23}
Median $\sigma_{T_{\text{eff}}}/T_{\text{eff}}$ (%)	0.93 ^{+1.16} _{-0.54}	1.07 ^{+1.32} _{-0.60}	0.69 ^{+1.45} _{-0.41}	0.50 ^{+0.67} _{-0.29}	0.90 ^{+1.27} _{-0.55}
Median $\sigma_{F_{\text{bol}}}/F_{\text{bol}}$ (%)	2.20 ^{+3.85} _{-1.57}	1.33 ^{+2.43} _{-0.87}	0.90 ^{+1.93} _{-0.58}	1.40 ^{+3.09} _{-0.97}	1.30 ^{+2.92} _{-0.91}
Median σ_θ/θ (%)	2.38 ^{+2.85} _{-1.42}	2.42 ^{+2.87} _{-1.35}	1.77 ^{+3.45} _{-1.02}	1.42 ^{+2.10} _{-0.86}	2.17 ^{+3.03} _{-1.32}
Median σ_{R_*}/R_* (%)	7.95 ^{+2.08} _{-2.68}	7.40 ^{+2.46} _{-2.76}	6.86 ^{+2.97} _{-3.11}	7.08 ^{+2.36} _{-2.88}	7.47 ^{+2.41} _{-3.01}

5. DISCUSSION

5.1. Radii of Low-mass Stars

We compare the radii derived for our cool stars to the radii predicted by the T_{eff} -radius relation given in Equation 9 of (Boyajian et al. 2012b). This relation is calibrated on a sample of 33 K- and M-dwarfs ($3200\text{K} \leq T_{\text{eff}} \leq 5500\text{K}$) plus the Sun, which is used as a bridge to extrapolate the relation to hotter stars. The relation, for stars with $T_{\text{eff}} > 3,200\text{K}$, is

$$R_*/R_\odot = -8.133(\pm 0.226) + 5.09342(\pm 0.16745) \times 10^{-3} T_{\text{eff}} \\ - 9.86602(\pm 0.40672) \times 10^{-7} T_{\text{eff}}^2 \\ + 6.47963(\pm 0.32429) \times 10^{-11} T_{\text{eff}}^3 \quad (6)$$

Figure 17 shows radius as a function of effective temperature for our stars, with the aforementioned relation plotted as the black line. We excluded giants from our comparison that were identified by either the $\log g_*$ cut or the reduced proper motion cut described in Section 5.2. We find good agreement over the calibrated temperature range between our dwarfs and this relation, even out to dwarfs hotter than the Sun. Additionally, the top panel shows the metal-poor stars sitting below the metal-rich stars on the main sequence and to the left of the metal-rich stars on the giant branch.

5.2. Limitations of the Iterative IRFM Technique

We note that our iterative IRFM technique has several limitations, and we caution the reader against unscrupulous application of the results presented in this paper. First and foremost, the IRFM relations from Casagrande et al. (2010) were calibrated using dwarfs and subgiants, so the resulting effective temperatures and bolometric fluxes for giants have not been verified. To this end, we identify stars with spectroscopic $\log g_* \leq 3$ as giants. For the stars without spectroscopic gravities, we use the *Gaia* DR1 proper motions and 2MASS *J*- and *H*-band photometry to calculate reduced proper motions. We then apply the reduced proper motion cut (Gould & Morgan 2003) as described by (Collier Cameron et al. 2007) to flag giants.

We also note that one could derive more accurate results for a given star if the extinction was known *a priori*, and that having extinctions for the nearly one million Tycho-2 stars

that were cut from our sample would enable us to estimate their temperatures, bolometric fluxes, angular diameters, and radii – given a precise enough TGAS astrometric solution.

Finally, as discussed in Section 4.1, the unscaled parameter uncertainties for the stars without spectroscopic priors are likely understated, given that the median uncertainties on T_{eff} (and thus the angular diameter) were a factor of two lower than for the stars with spectroscopic priors. This is because our χ^2 merit function includes a nonnegative penalty for the stars with spectroscopic T_{eff} priors, so when we re-scale the T_{eff} uncertainties to force $\chi^2_\nu = 1$, this scale factor is larger for the stars with T_{eff} priors than for those without. Thus, for each star with a spectroscopic T_{eff} we run our analysis with and without applying a T_{eff} prior (and penalty); bin the stars according to the IRFM T_{eff} determined without applying the prior; find the ratio of the median uncertainties on the parameters with and without the prior; partition the stars without spectroscopic T_{eff} values into the same T_{eff} bins; and scale the uncertainties by these ratios. We can compare this approach to the uncertainties determined from full SED fits, which we will perform in future work.

6. CONCLUSION

We have determined effective temperatures, bolometric fluxes and angular diameters for over 1.6 million *Tycho-2* stars plus linear radii for 355,502 of these stars that have $< 10\%$ *Gaia* parallaxes. We demonstrate the ability to create the theorists' HR diagram directly from measured quantities using a substantially larger set of stars than were available in the *Hipparcos* era. This is the largest collection of empirical stellar angular diameters and radii and should thus serve as a canonical sample for stellar and exoplanetary investigations as outlined in the introduction.

Now, in the era of precision astronomy enabled by *Gaia*, we have the opportunity to determine the fundamental parameters of a large sample of stars *empirically* and to considerably tighter precision and accuracy than has previously been possible. Because $\sigma_{R_*}/R_* \sim 2\sigma_{T_{\text{eff}}}/T_{\text{eff}}$ (when T_{eff} uncertainties dominate all other sources of error) and because our knowledge of the extinction to each star is *a priori* poor, the uncertainties on effective temperature and extinction will fundamentally limit our ability to measure the radii precisely and accurately if *Gaia* reaches its expected end-of-mission astrometric precision of $\sim 10\mu$ as for bright stars. We need precise (several percent or better) effective temperatures – of order the precision quoted by Brewer et al. (2016) for $\sim 1,600$ F, G, and K stars – and we need to resolve the discrepancies and systematic offsets between different methods of inferring stellar effective temperature (cf. Boyajian et al. 2012b).

In the next few years, there are great prospects both for dramatically increasing the sample of stars with precise radii and for improving the precision on these radii. *Gaia*'s improved precision and expanded astrometric catalog will yield a considerably larger and more precise set of stellar radii, with potentially more than 600,000 stars with parameters derived from our iterative IRFM technique presented here. The release of either *Gaia* effective temperatures or the blue-pass and red-pass spectrophotometry slated for 2018 will also en-

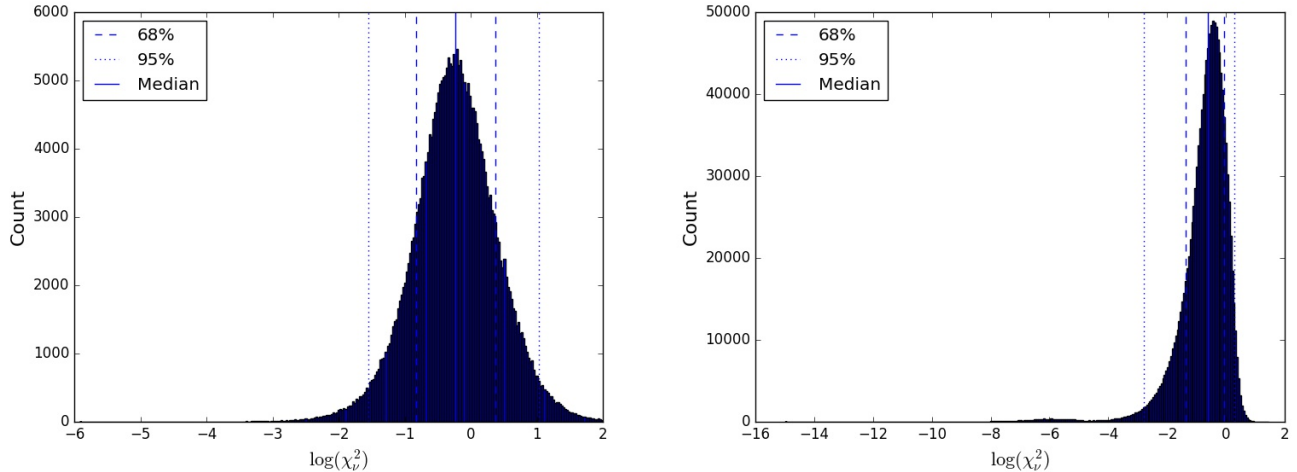


Figure 10. $\log \chi^2$ distributions for the stars with spectroscopic parameters (left) and without (right). In each panel, the solid line denoted the median value, the dashed lines denote the 68% interval, and the dotted lines denote the 95% interval.

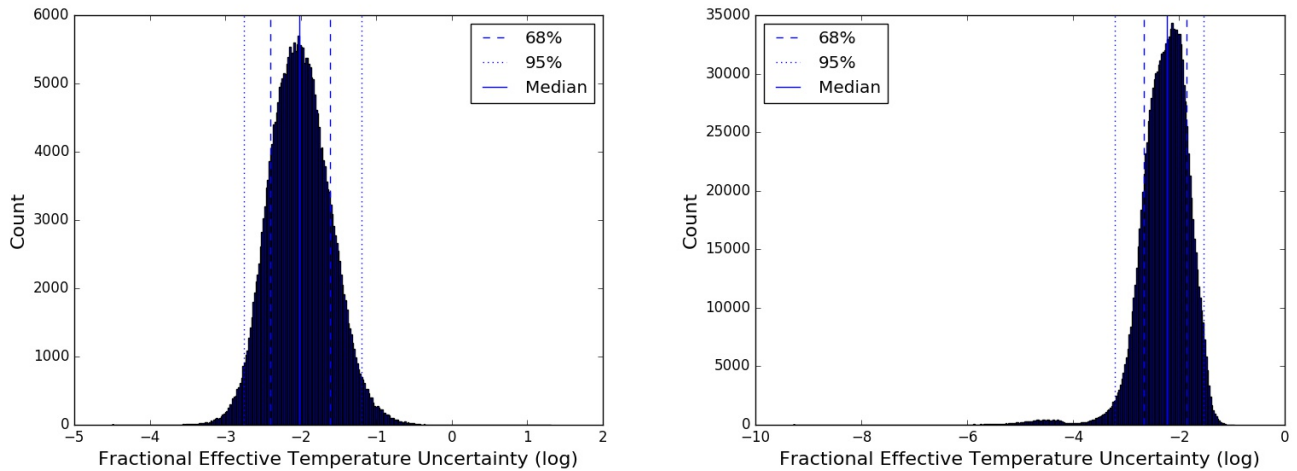


Figure 11. Histograms showing the fractional precision on the effective temperature for the stars with spectroscopic parameters (left) and without (right). In each panel, the solid line denoted the median value, the dashed lines denote the 68% interval, and the dotted lines denote the 95% interval.

able us to expand our sample to include stars for which this information is made available.

The BP/RP spectrophotometry in particular will make precise SED modeling possible, particularly for AFGK stars whose SEDs peak in the 330-1050nm range of the BP/RP filters. Combining literature broad-band photometry, *Gaia* spectrophotometry, and spectrophotometry from $\sim 0.75 - 5\mu\text{m}$ from the proposed SPHEREx mission (Doré et al. 2016) will capture nearly all the flux for these stars, cover the SED peaks for later-type stars, and enable direct measurements of the line-of-sight extinction as a function of wavelength, without reliance on previously calibrated extinction laws.

Work by B.S.G. and D.J.S was partially supported by NSF CAREER Grant AST-1056524. D.J.S. thanks R. Oelkers for assistance querying the TGAS catalog; J. Birkby, C. Dressing, J. Johnson, M. Pinsonneault, J. Tayar, A. Vanderburg,

and J. Yee for fruitful scientific discussion and S. Kim, M. Penny, and D. Will for computational advice.

This work has made use of NASA’s Astrophysics Data System, the SIMBAD database operated at CDS, Strasbourg, France, the VizieR catalogue access tool, CDS, Strasbourg, France (Ochsenbein et al. 2000), and the Two Micron All Sky Survey, which is a joint project of the University of Massachusetts and the Infrared Processing and Analysis Center/California Institute of Technology, funded by the National Aeronautics and Space Administration and the National Science Foundation.

The research described in this paper makes use of Filtergraph, an online data visualization tool developed at Vanderbilt University through the Vanderbilt Initiative in Data-intensive Astrophysics (VIDA; Burger et al. 2013).

Funding for the Sloan Digital Sky Survey IV has been provided by the Alfred P. Sloan Foundation, the U.S. Department of Energy Office of Science, and the Participating In-

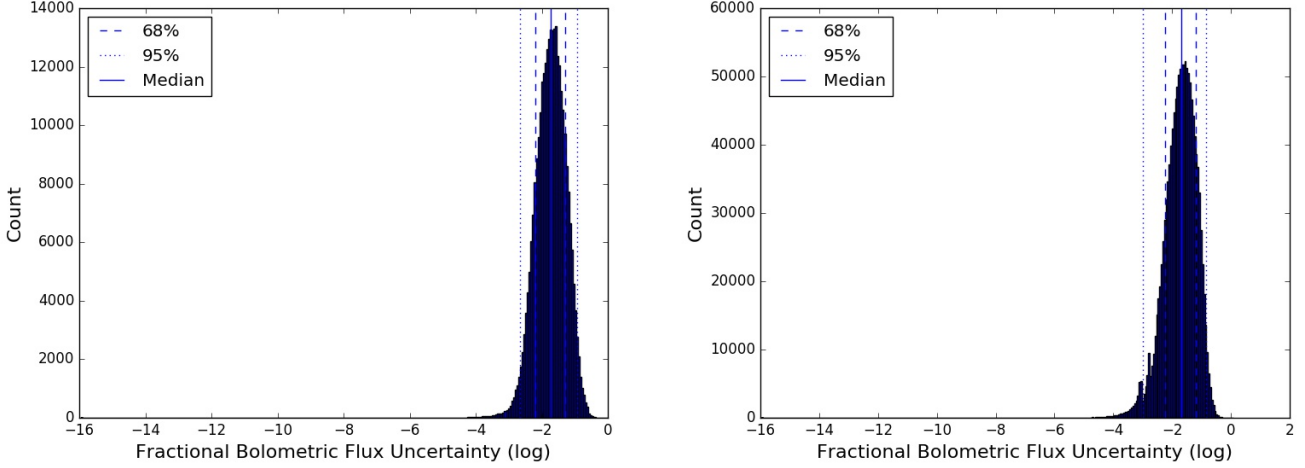


Figure 12. Histograms showing the fractional precision on the bolometric flux for the stars with spectroscopic parameters (left) and without (right). In each panel, the solid line denoted the median value, the dashed lines denote the 68% interval, and the dotted lines denote the 95% interval.

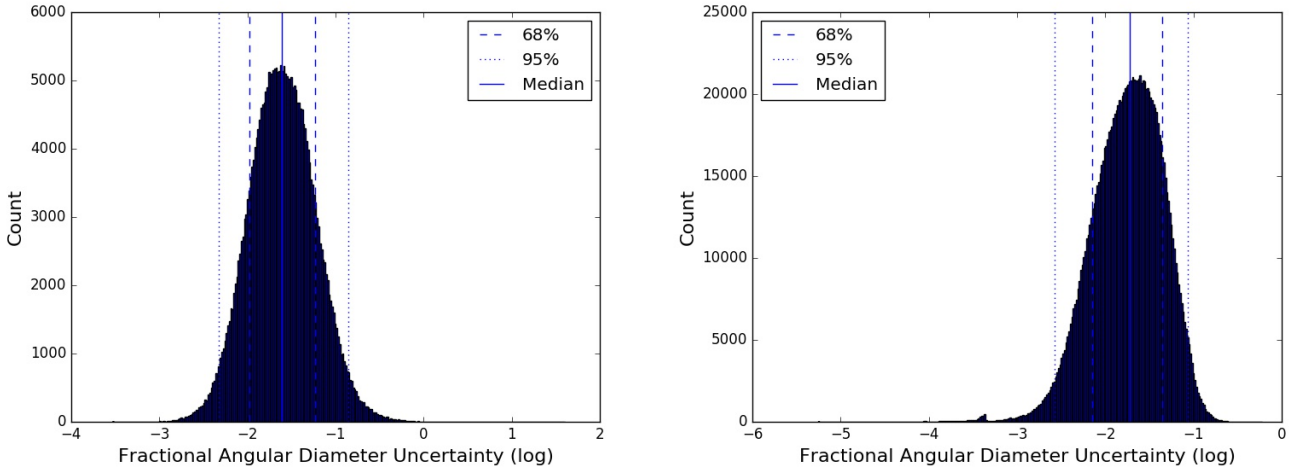


Figure 13. Histograms showing the fractional precision on the angular diameter for the stars with spectroscopic parameters (left) and without (right). In each panel, the solid line denoted the median value, the dashed lines denote the 68% interval, and the dotted lines denote the 95% interval.

stitutions. SDSS acknowledges support and resources from the Center for High-Performance Computing at the University of Utah. The SDSS web site is www.sdss.org.

Funding for RAVE has been provided by: the Australian Astronomical Observatory; the Leibniz-Institut fuer Astrophysik Potsdam (AIP); the Australian National University; the Australian Research Council; the French National Research Agency; the German Research Foundation (SPP 1177 and SFB 881); the European Research Council (ERC-StG 240271 Galactica); the Istituto Nazionale di Astrofisica at

Padova; The Johns Hopkins University; the National Science Foundation of the USA (AST-0908326); the W. M. Keck foundation; the Macquarie University; the Netherlands Research School for Astronomy; the Natural Sciences and Engineering Research Council of Canada; the Slovenian Research Agency; the Swiss National Science Foundation; the Science & Technology Facilities Council of the UK; Opticon; Strasbourg Observatory; and the Universities of Groningen, Heidelberg and Sydney. The RAVE web site is located at <https://www.rave-survey.org>.

REFERENCES

- Bianchi, L., Herald, J., Efremova, B., et al. 2011, *Ap&SS*, 335, 161
 Birkby, J., Nefs, B., Hodgkin, S., et al. 2012, *MNRAS*, 426, 1507
 Blanton, M. R., Bershady, M. A., Abolfathi, B., et al. 2017, *ArXiv e-prints*, arXiv:1703.00052
 Boyajian, T. S., van Belle, G., & von Braun, K. 2014, *AJ*, 147, 47
 Boyajian, T. S., McAlister, H. A., van Belle, G., et al. 2012a, *ApJ*, 746, 101
 Boyajian, T. S., von Braun, K., van Belle, G., et al. 2012b, *ApJ*, 757, 112

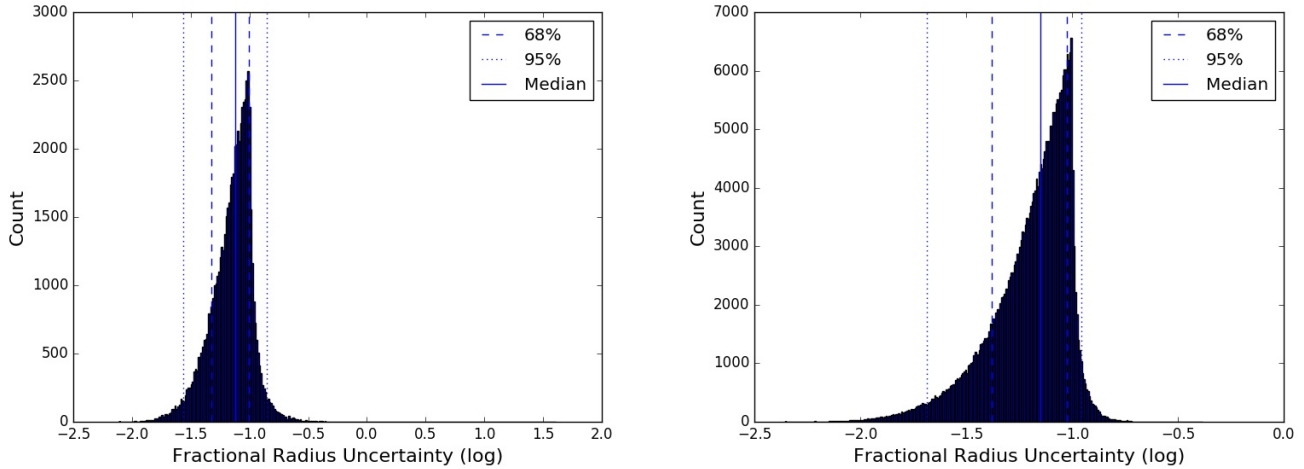


Figure 14. Histograms showing the fractional precision on the radius for the subset of stars with spectroscopic parameters (left) and without (right) that have precise TGAS parallaxes. In each panel, the solid line denoted the median value, the dashed lines denote the 68% interval, and the dotted lines denote the 95% interval. The effect of our parallax precision cut manifests as a large drop-off around 10%.

- Brewer, J. M., Fischer, D. A., Valenti, J. A., & Piskunov, N. 2016, *ApJS*, 225, 32
- Burger, D., Stassun, K. G., Pepper, J., et al. 2013, *Astronomy and Computing*, 2, 40
- Campante, T. L., Schofield, M., Kuzlewicz, J. S., et al. 2016, *ArXiv e-prints*, arXiv:1608.01138
- Cardelli, J. A., Clayton, G. C., & Mathis, J. S. 1989, *ApJ*, 345, 245
- Casagrande, L., Ramírez, I., Meléndez, J., Bessell, M., & Asplund, M. 2010, *A&A*, 512, A54
- Casagrande, L., Schönrich, R., Asplund, M., et al. 2011, *A&A*, 530, A138
- Casertano, S., Riess, A. G., Bucciarelli, B., & Lattanzi, M. G. 2017, *A&A*, 599, A67
- Collier Cameron, A., Wilson, D. M., West, R. G., et al. 2007, *MNRAS*, 380, 1230
- Cutri, R. M., & et al. 2014, *VizieR Online Data Catalog*, 2328
- Cutri, R. M., Skrutskie, M. F., van Dyk, S., et al. 2003, *VizieR Online Data Catalog*, 2246
- Doré, O., Werner, M. W., Ashby, M., et al. 2016, *ArXiv e-prints*, arXiv:1606.07039
- Gaia Collaboration. 2016, *ArXiv e-prints*, arXiv:1609.04153
- Gaia Collaboration, Brown, A. G. A., Vallenari, A., et al. 2016, *ArXiv e-prints*, arXiv:1609.04172
- Gould, A., Kollmeier, J. A., & Sesar, B. 2016, *ArXiv e-prints*, arXiv:1609.06315
- Gould, A., & Morgan, C. W. 2003, *ApJ*, 585, 1056
- Høg, E., Fabricius, C., Makarov, V. V., et al. 2000, *A&A*, 355, L27
- Kordopatis, G., Gilmore, G., Steinmetz, M., et al. 2013, *AJ*, 146, 134
- Kurucz, R. L. 2013, *ATLAS12: Opacity sampling model atmosphere program*, *Astrophysics Source Code Library*, , ascl:1303.024
- Lindgren, L., Lammers, U., Bastian, U., et al. 2016, *ArXiv e-prints*, arXiv:1609.04303
- Luo, A.-L., Zhao, Y.-H., Zhao, G., et al. 2015, *Research in Astronomy and Astrophysics*, 15, 1095
- Lutz, T. E., & Kelker, D. H. 1973, *PASP*, 85, 573
- Mann, A. W., Feiden, G. A., Gaidos, E., Boyajian, T., & von Braun, K. 2015, *ApJ*, 804, 64
- Mermilliod, J. C. 2006, *VizieR Online Data Catalog*, 2168
- Ochsenbein, F., Bauer, P., & Marcout, J. 2000, *A&AS*, 143, 23
- Paunzen, E. 2015, *A&A*, 580, A23
- Perryman, M. A. C., Lindgren, L., Kovalevsky, J., et al. 1997, *A&A*, 323, L49
- Rauer, H., Catala, C., Aerts, C., et al. 2014, *Experimental Astronomy*, 38, 249
- Ricker, G. R., Winn, J. N., Vanderspek, R., et al. 2015, *Journal of Astronomical Telescopes, Instruments, and Systems*, 1, 014003
- Schlegel, D. J., Finkbeiner, D. P., & Davis, M. 1998, *ApJ*, 500, 525
- SDSS Collaboration, Albareti, F. D., Allende Prieto, C., et al. 2016, *ArXiv e-prints*, arXiv:1608.02013
- Skrutskie, M. F., Cutri, R. M., Stiening, R., et al. 2006, *AJ*, 131, 1163
- Somers, G., & Stassun, K. G. 2016, *ArXiv e-prints*, arXiv:1609.04841
- Stassun, K. G., Collins, K. A., & Gaudi, B. S. 2016, *ArXiv e-prints*, arXiv:1609.04389
- Stassun, K. G., Feiden, G. A., & Torres, G. 2014a, *NewAR*, 60, 1
- Stassun, K. G., Kratter, K. M., Scholz, A., & Dupuy, T. J. 2012, *ApJ*, 756, 47
- Stassun, K. G., Pepper, J. A., Oelkers, R., et al. 2014b, *ArXiv e-prints*, arXiv:1410.6379
- Stassun, K. G., & Torres, G. 2016a, *ArXiv e-prints*, arXiv:1609.02579
- . 2016b, *ArXiv e-prints*, arXiv:1609.05390
- Stassun, K. G., Oelkers, R. J., Pepper, J., et al. 2017, *ArXiv e-prints*, arXiv:1706.00495
- Torres, G., Andersen, J., & Giménez, A. 2010, *A&A Rv*, 18, 67

APPENDIX

A. SPECTRAL ENERGY DISTRIBUTIONS

In Figure Set A1 we present the observed and fitted spectral energy distributions of the 244 Casagrande et al. (2010) stars with which we test the iterative IRFM method employed to determine effective temperatures, bolometric fluxes, and angular diameters for the full study sample.

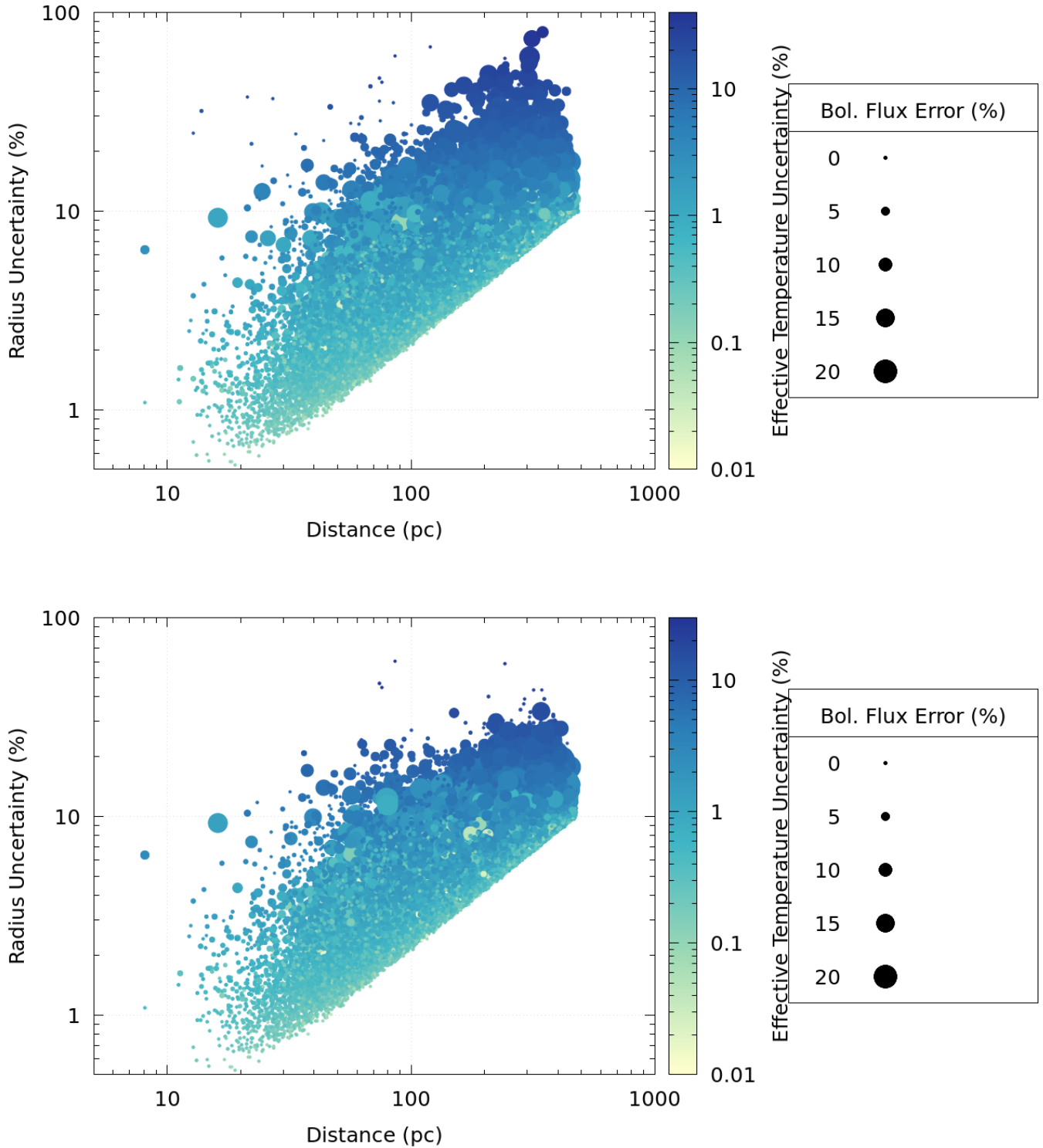


Figure 15. Fractional radius uncertainty as a function of *Gaia* parallax distance for the stars with spectroscopic parameters (top) and without (bottom). The points are color-coded by the fractional effective temperature uncertainty and sized by the fractional bolometric flux uncertainty; for presentation purposes, we only plot stars with $< 20\%$ bolometric flux uncertainties. The parallax uncertainties set the floor of the radius uncertainties, and a strong vertical color gradient highlights the effective temperature uncertainty's dominance on the radius error budget.

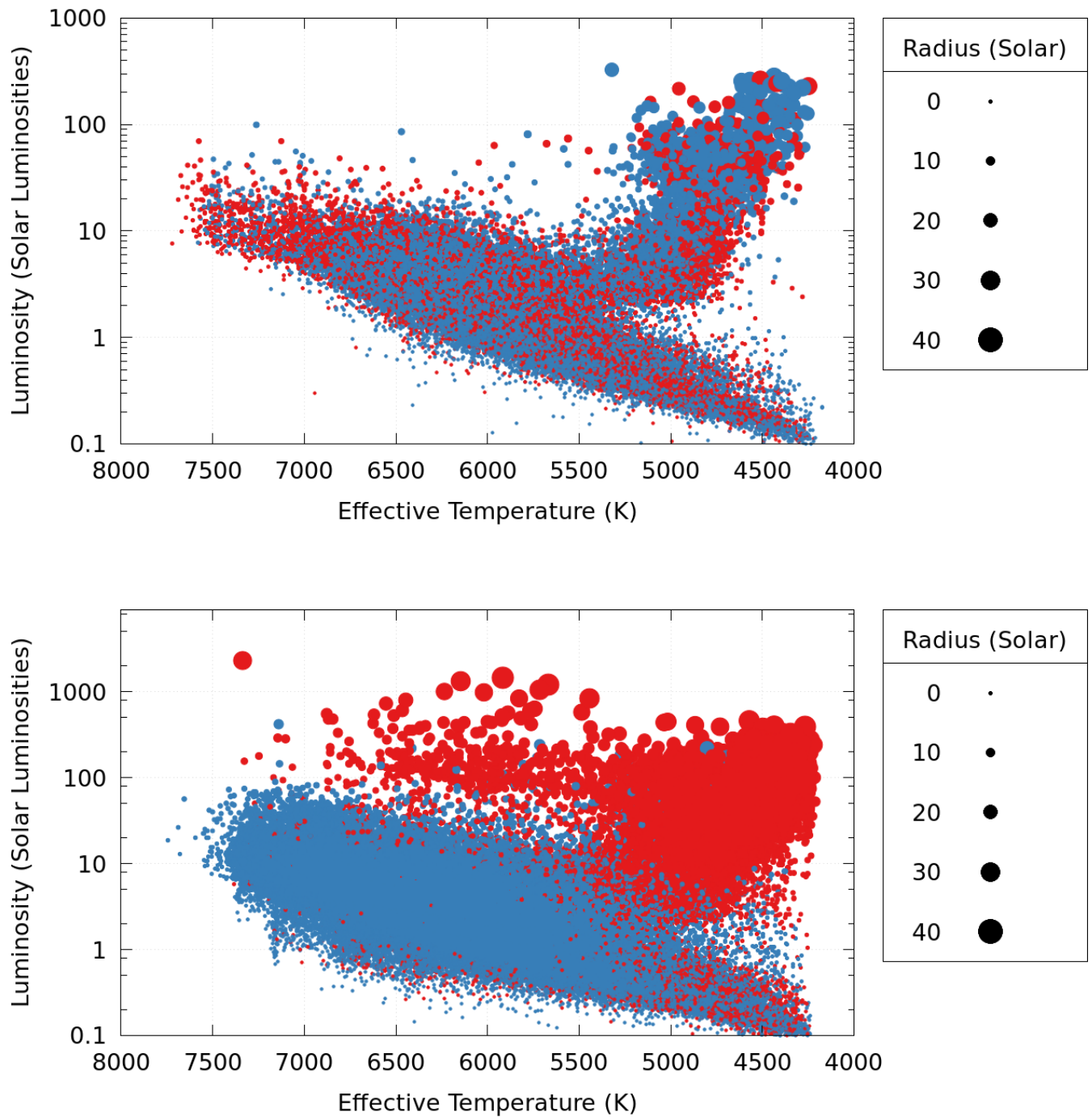


Figure 16. Theoretical HR diagrams for the subsample of stars with $< 10\%$ *Gaia* parallaxes, with (top) and without (bottom) spectroscopic parameters. The top panel is color-coded by metallicity such that stars with $[Fe/H] > 0$ are red and stars with $[Fe/H] < 0$ are blue. In the bottom panel, the stars that the reduced proper motion cut identifies as dwarfs are in blue, while the rest are in red. Point size increases with radius. For presentation purposes, we show only stars with $L_{bol} > 0.1 L_{bol,\odot}$. In both panels, a cluster of cool, evolved stars distinguishes itself from the main sequence. We note that the cluster of hot, luminous stars to the upper-left of the non-spectroscopic HR diagram, which reflects the limitations of our technique for stars $> 7,000K$.

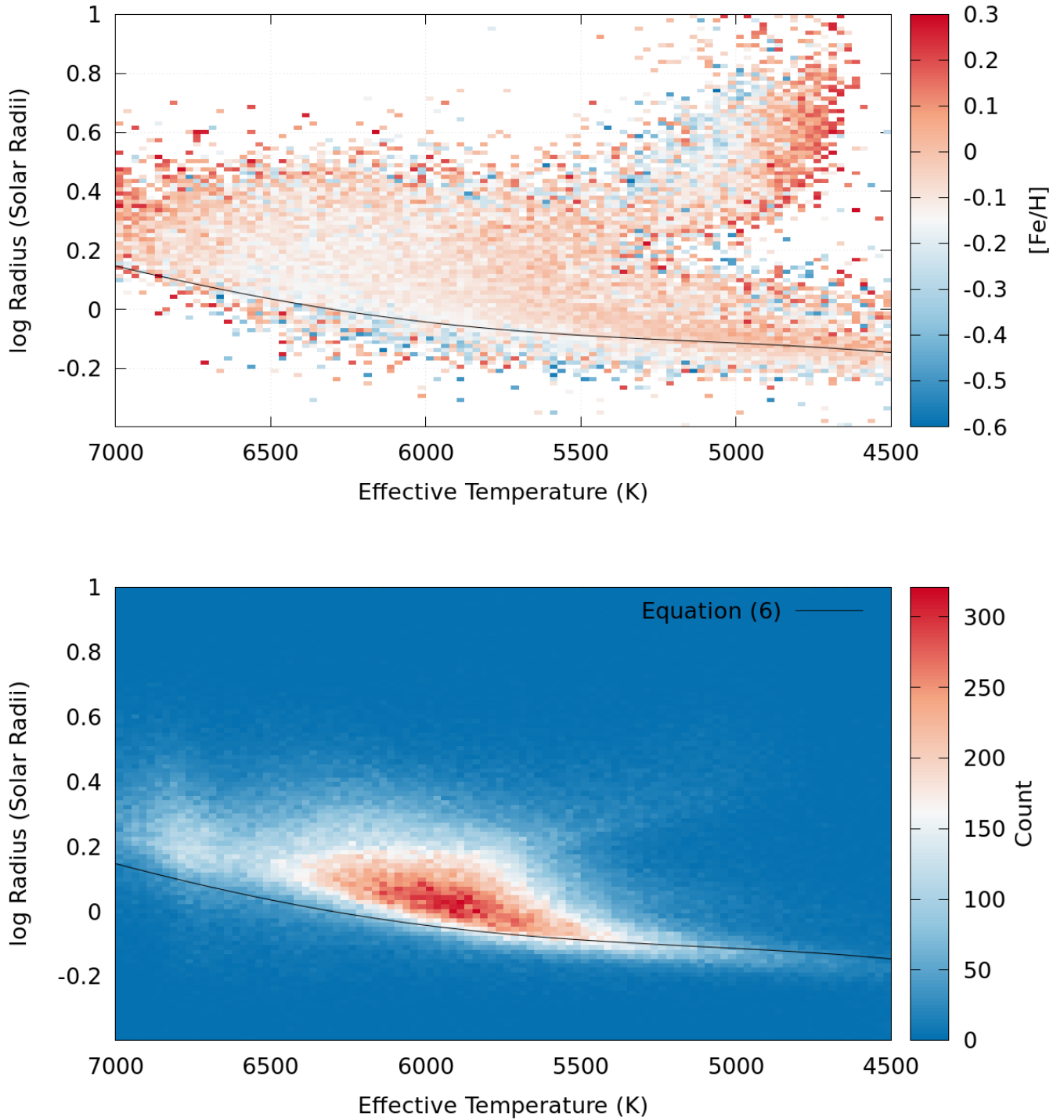


Figure 17. Radius as a function of effective temperature for the spectroscopic (top) and non-spectroscopic (bottom) star samples. The top panel is restricted to stars with a $\log g_* > 3$, while the bottom panel is restricted to stars identified as dwarfs by the reduced proper motion cut. The black line is the relation given by Equation 6 (Equation 9 of [Boyajian et al. 2012b](#)).

Table 4. Catalog Photometry for 1,600,080 Tycho-2 Stars Used in Iterative-IRFM Routine

Star	RA (J2000)	Dec (J2000)	B_T	σ_{B_T}	V_T	σ_{V_T}	J	σ_J	H	σ_H	K_S	σ_{K_S}	B	σ_B	V	σ_V	b	σ_b	y	σ_y
TYC 100-1166-1	80.01164972	1.12232972	12.512	0.236	11.850	0.188	10.262	0.026	9.748	0.022	9.639	0.021
TYC 1001-1885-1	264.45634000	11.68801222	8.644	0.017	8.296	0.013	7.578	0.018	7.464	0.027	7.413	0.024	8.477	0.0084852814	8.274	0.0006
TYC 100-1394-1	79.922395889	1.58643111	12.071	0.149	11.166	0.098	10.106	0.022	9.677	0.022	9.597	0.019
TYC 1003-2217-1	261.87815972	13.35782833	12.521	0.239	12.296	0.239	10.952	0.021	10.717	0.018	10.649	0.018
TYC 1004-1638-1	264.19612222	14.86987694	12.489	0.220	11.794	0.173	9.610	0.022	8.983	0.020	8.837	0.017
TYC 1004-1657-1	263.96095722	14.04696917	12.761	0.268	11.604	0.135	9.311	0.027	8.690	0.053	8.528	0.022
TYC 1004-1680-1	263.91493167	14.72536222	12.986	0.322	12.013	0.202	9.762	0.027	9.048	0.030	8.919	0.019
TYC 1004-1777-1	262.51756000	14.46246167	9.190	0.018	8.586	0.013	7.443	0.021	7.222	0.042	7.153	0.026	8.896	0.004	8.52	0
TYC 1005-1574-1	265.36997972	14.72544194	12.604	0.233	11.451	0.109	9.563	0.020	9.033	0.019	8.877	0.017
TYC 1005-1908-1	264.85883750	14.96200306	12.156	0.144	11.637	0.132	9.834	0.021	9.286	0.020	9.185	0.017

NOTE—Table 4 is published in its entirety in the machine-readable format. A portion is shown here for guidance regarding its form and content.

Table 5. Fundamental Parameters of 1,600,080 *Tycho-2* Stars

Star	$\log \chi^2_\nu$ (unscaled)	A_V	σ_{A_V}	T_{eff} (K)	$\sigma_{T_{\text{eff}}}$ (K)	$\log F_{\text{bol}}$ ($\text{erg cm}^{-2} \text{s}^{-1}$)	$\log \sigma_{F_{\text{bol}}}$ ($\text{erg cm}^{-2} \text{s}^{-1}$)	θ (μas)	σ_θ (μas)	$T_{\text{eff,spec}}$ (K)	$\sigma_{T_{\text{eff,spec}}}$ (K)	[Fe/H]	$\sigma_{[\text{Fe}/\text{H}]}$	$\log(g)$	$\sigma_{\log(g)}$	Spec. Source	Hot Flag ¹
TYCI023-508-1	-0.432	0.180	0.040	5178.050	11.581	-7.391	-9.517	412.046	2.490	5157	69	-0.375488	0.0313319	3.33086	0.08	APOGEE	0
TYCI035-1205-1	-1.334	0.710	0.010	4277.800	15.351	-8.689	-10.573	135.396	1.363	4307	69	-0.311677	0.030143	1.70132	0.08	APOGEE	0
TYCI038-1289-1	-1.045	1.000	0.030	4347.820	14.452	-8.366	-9.621	190.233	5.522	4347	69	0.0579264	0.0229669	2.24876	0.08	APOGEE	0
TYCI-1024-1	-0.231	0.104	0.054	6261.670	54.544	-8.793	-10.380	56.057	1.251	6431	189	0.044	0.333	4.116	0.438	LAMOST	0
TYCI-1111-1	-0.274	0.000	0.040	5721.840	78.121	-9.191	-11.362	42.456	1.177	5665	218	-0.502	0.582	4.535	0.535	LAMOST	0
TYCI-1122-1	0.144	0.087	0.067	5810.800	78.816	-8.815	-10.141	63.478	2.348	6020	207	0.106	0.396	4.516	0.493	LAMOST	0
TYCI000-1006-1	-1.122	0.000	0.006	6618.690	35.803	-8.775	-11.256	51.211	0.562	0
TYCI000-1009-1	-0.387	0.413	0.022	5934.640	134.770	-9.218	-10.728	38.247	1.846	0
TYCI000-1016-1	-5.422	0.260	0.007	6952.350	1.070	-8.742	-11.972	48.240	0.021	0
TYCI00-1166-1	-0.125	0.070	0.110	5064.370	88.065	-9.185	-10.574	54.568	2.220	5110	105	-0.08	0.09	3.34	0.21	RAVE	0
TYCI00-1394-1	1.390	0.000	0.050	5869.290	454.894	-9.028	-10.485	48.703	7.613	5148	66	0.05	0.09	3.63	0.1	RAVE	0
TYCI0-1118-1	0.299	0.000	0.020	6016.600	136.251	-9.048	-10.384	45.262	2.319	5784	95	-0.01	0.1	4.16	0.15	RAVE	0

¹ "1" indicates $T_{\text{eff}} > 7,000$ K for which the iterative IRFM parameters may not be reliable – see Section 3.2.2.

NOTE.—Table 5 is published in its entirety in the machine-readable format. A portion is shown here for guidance regarding its form and content.

Table 6. Fundamental Parameters of 355,502 TGAS Stars with Radii

Star	$\log \chi^2_{\nu}$ (unscaled)	A_V	σ_{A_V}	T_{eff} (K)	$\sigma_{T_{\text{eff}}}$ (K)	$\log F_{\text{bol}}$ ($\text{erg cm}^{-2} \text{s}^{-1}$)	$\log \sigma_{F_{\text{bol}}}$ ($\text{erg cm}^{-2} \text{s}^{-1}$)	θ (μas)	σ_{θ} (μas)	Parallax (mas)	Error (mas)	d (pc)	σ_d (pc)	R_* (R_{\odot})	σ_{R_*} (R_{\odot})	$T_{\text{eff,spec}}$ (K)	$\sigma_{T_{\text{eff,spec}}}$ (K)	[Fe/H]	$\sigma_{[\text{Fe}/\text{H}]}$	Giant Flag ¹	Spec. Source
TYC1023-508-1	-0.432	0.180	0.040	5178.049	11.581	-7.391	-9.517	412.047	2.819	12.154	0.369	82.279	2.497	3.645	0.113	5157	69	-0.375488	0.0313319	0	APOGEE
TYC1045-202-1	-3.246	0.470	0.010	7205.317	3.387	-8.283	-11.062	76.162	0.112	3.902	0.346	256.282	22.695	2.099	0.186	7207	69	-0.094537	0.00807948	0	APOGEE
TYC1046-562-1	-0.224	0.000	0.010	6714.853	33.323	-8.419	-10.473	74.988	0.924	4.153	0.289	240.780	16.776	1.941	0.137	6652	69	-0.35377	0.0106944	0	APOGEE
TYC1-1122-1	0.144	0.087	0.067	5810.803	78.816	-8.815	-10.141	63.478	2.252	6.687	0.446	149.537	9.967	1.021	0.077	6020	207	0.106	0.396	0	LAMOST
TYC1-1167-1	-1.050	0.099	0.019	6404.499	15.014	-8.247	-10.275	100.556	0.657	5.868	0.290	170.409	8.412	1.842	0.092	6412	222	-0.539	0.537	0	LAMOST
TYC1120-184-1	0.100	0.187	0.017	6382.752	44.454	-8.160	-10.484	111.881	1.574	10.413	0.260	96.035	2.401	1.155	0.033	6461	64	0.383	0.122	0	LAMOST
TYC1000-1018-1	-0.745	0.130	0.056	6204.678	92.669	-9.223	-10.690	34.828	1.253	2.875	0.269	347.823	32.578	1.302	0.131	0	...
TYC1000-1123-1	-0.786	0.000	0.015	6072.540	56.676	-9.033	-10.768	45.210	0.981	3.933	0.230	254.245	14.890	1.236	0.077	0	...
TYC1000-1138-1	-0.070	0.130	0.030	6222.277	71.453	-8.615	-10.121	69.664	2.032	7.922	0.727	126.236	11.587	0.946	0.091	0	...
TYC1072-2400-1	0.520	0.000	0.010	6214.807	47.166	-7.217	-9.661	349.431	5.352	16.276	0.434	61.441	1.638	2.308	0.071	5960	67	-0.13	0.09	0	RAVE
TYC1-1058-1	0.389	0.000	0.030	5578.937	95.636	-8.923	-11.155	60.795	2.095	7.597	0.504	131.637	8.727	0.860	0.064	5052	145	-0.35	0.12	0	RAVE
TYC1138-130-1	0.306	0.010	0.010	6539.489	44.563	-7.046	-9.322	384.006	5.350	31.803	0.519	31.444	0.513	1.298	0.028	6250	82	-0.21	0.11	0	RAVE

NOTE—Table 6 is published in its entirety in the machine-readable format. A portion is shown here for guidance regarding its form and content.

¹ "0" if not identified as a giant (either via spectroscopic $\log g_*$ or reduced proper motion), "1" if so, and "2" if data are unavailable.

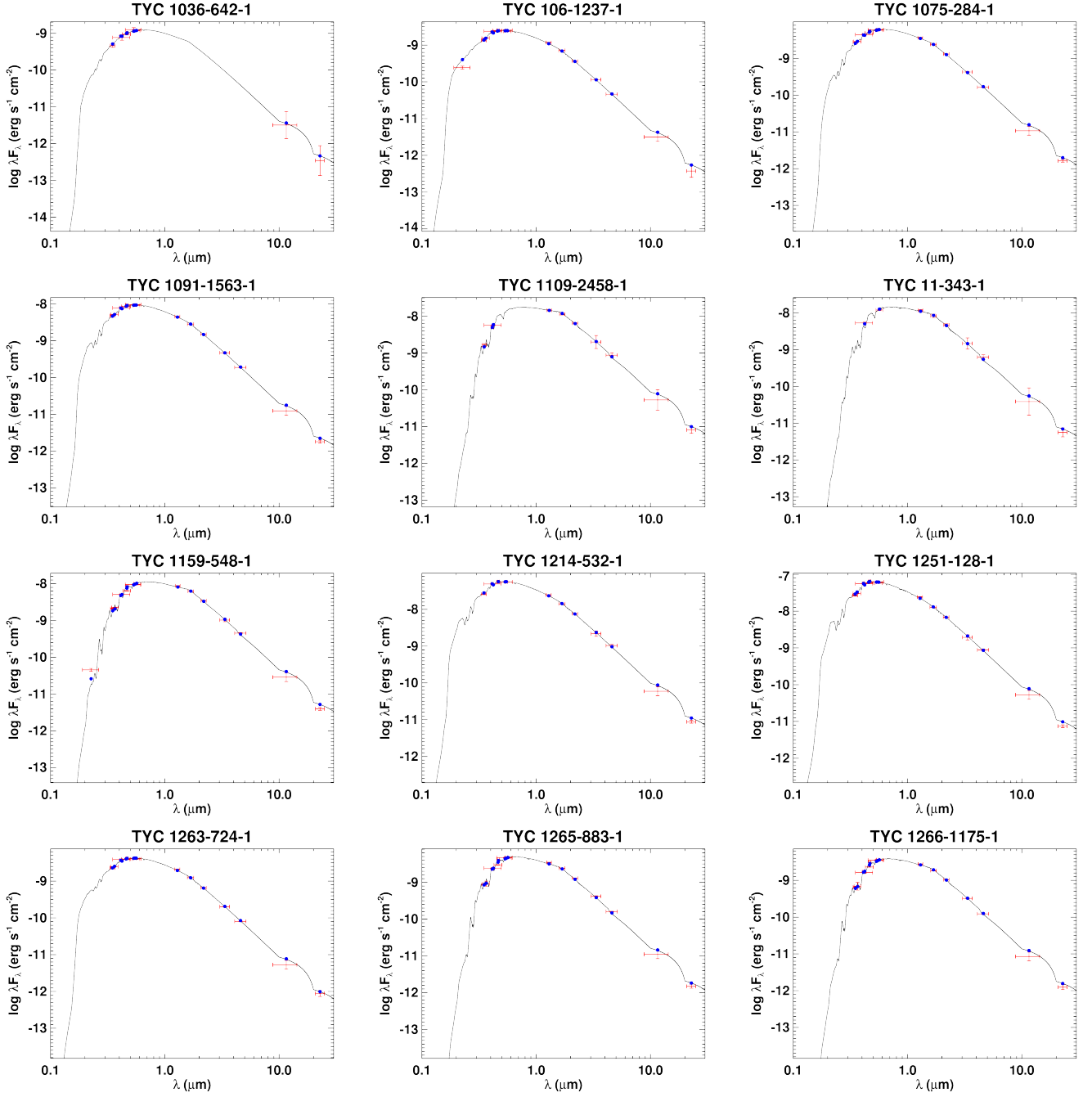


Figure A1. Spectral energy distributions (SEDs) for the 244 stars in the [Casagrande et al. \(2010\)](#) sample that also have iterative IRFM solutions. The black curve shows the model fit, while the blue crosses show the measured fluxes: the vertical bars denote the uncertainties on the measurements and the horizontal bars denote the width of the corresponding filter. The blue dots denote the model flux in that passband.

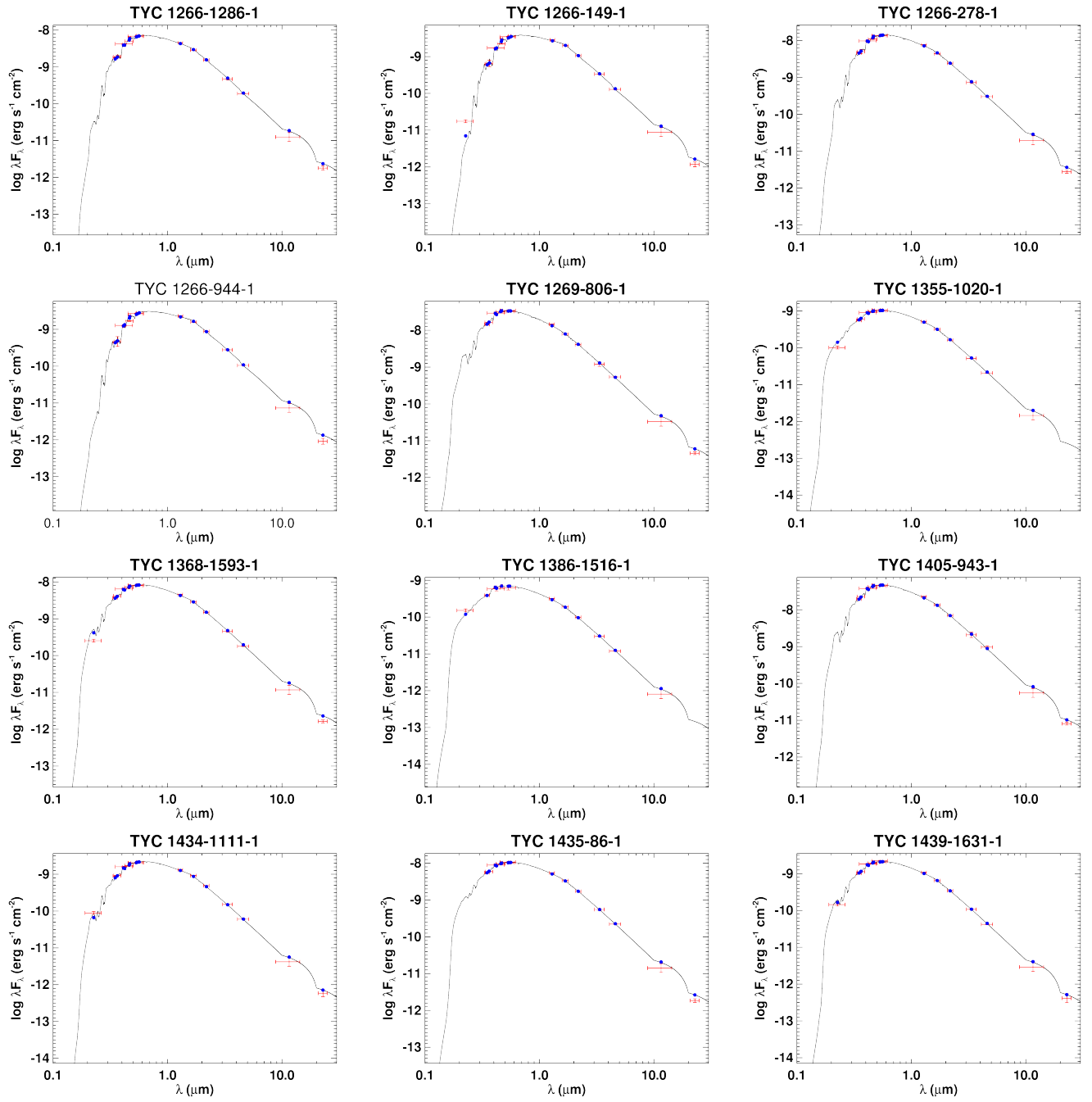


Figure A2. All labels, lines, symbols, and colors as in Figure A1.

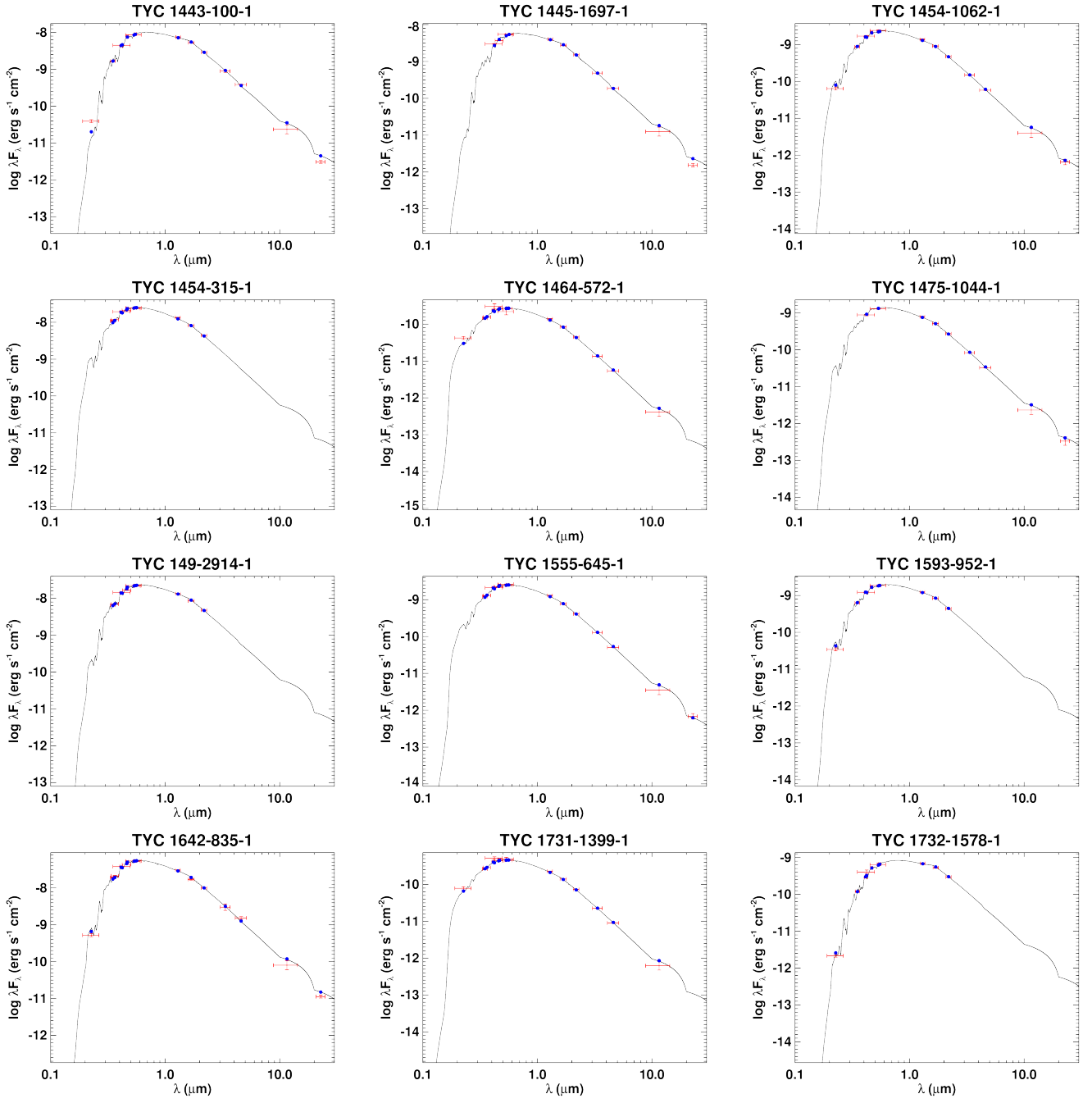


Figure A3. All labels, lines, symbols, and colors as in Figure A1.

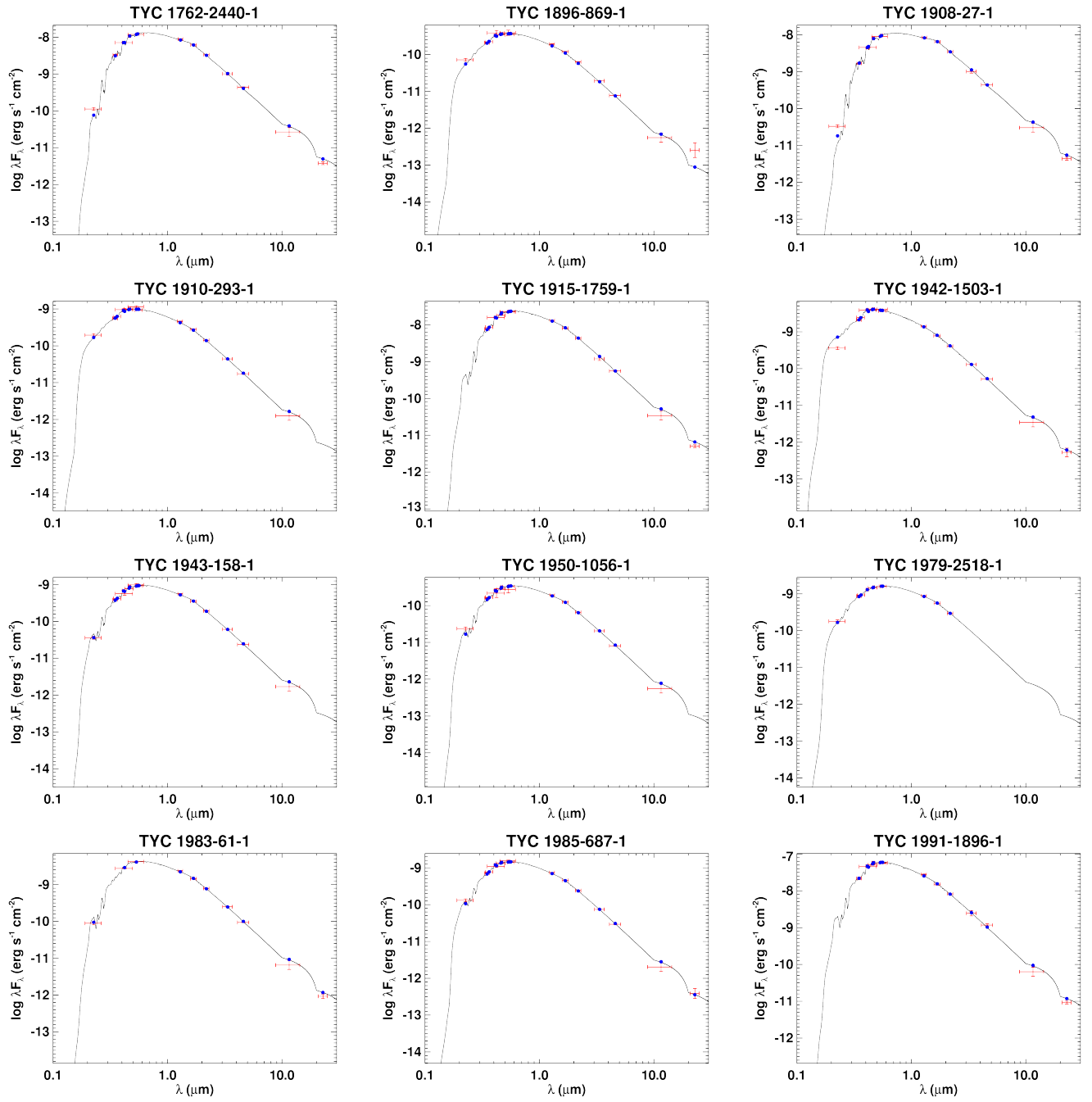


Figure A4. All labels, lines, symbols, and colors as in Figure A1.

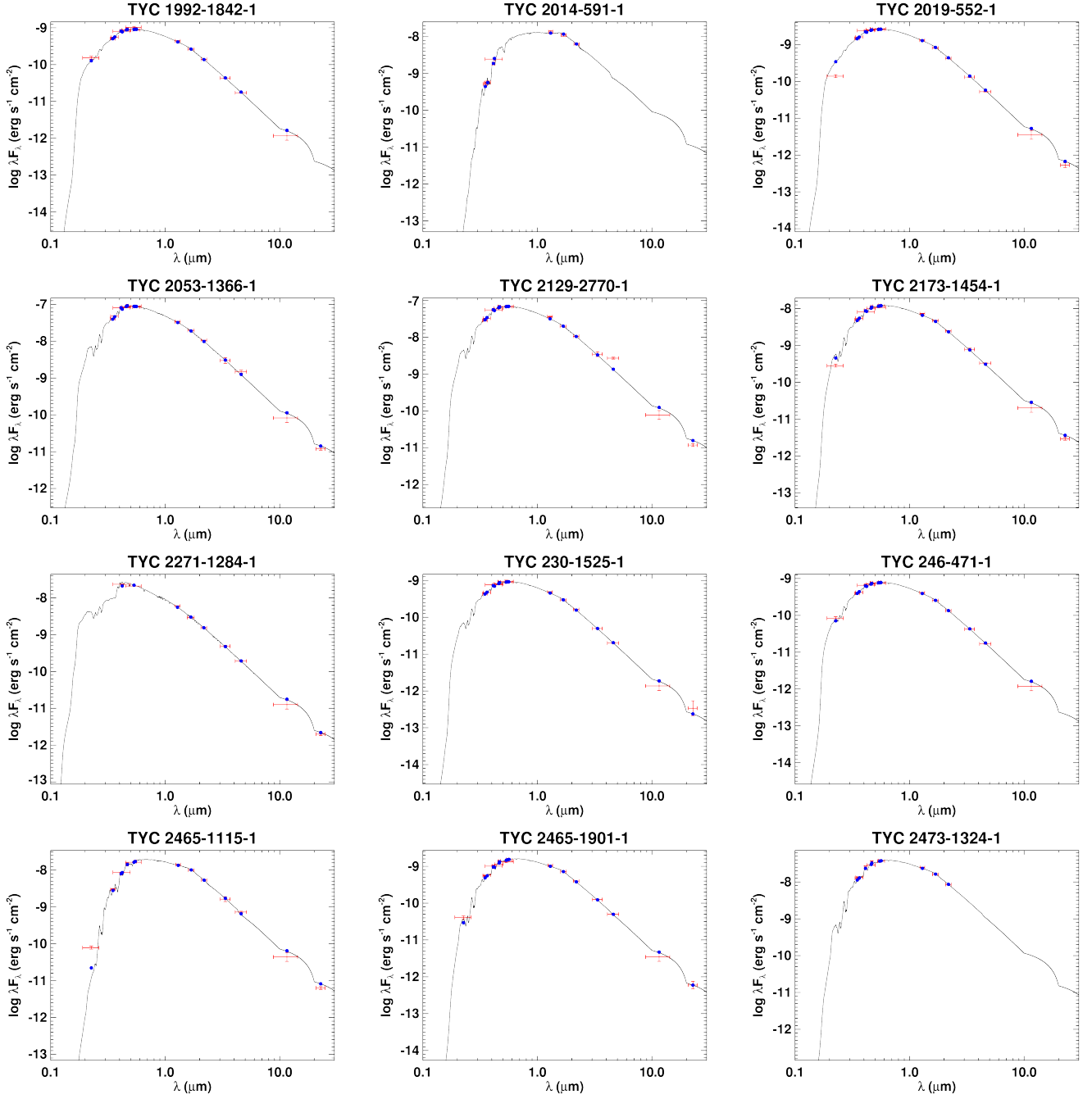


Figure A5. All labels, lines, symbols, and colors as in Figure A1.

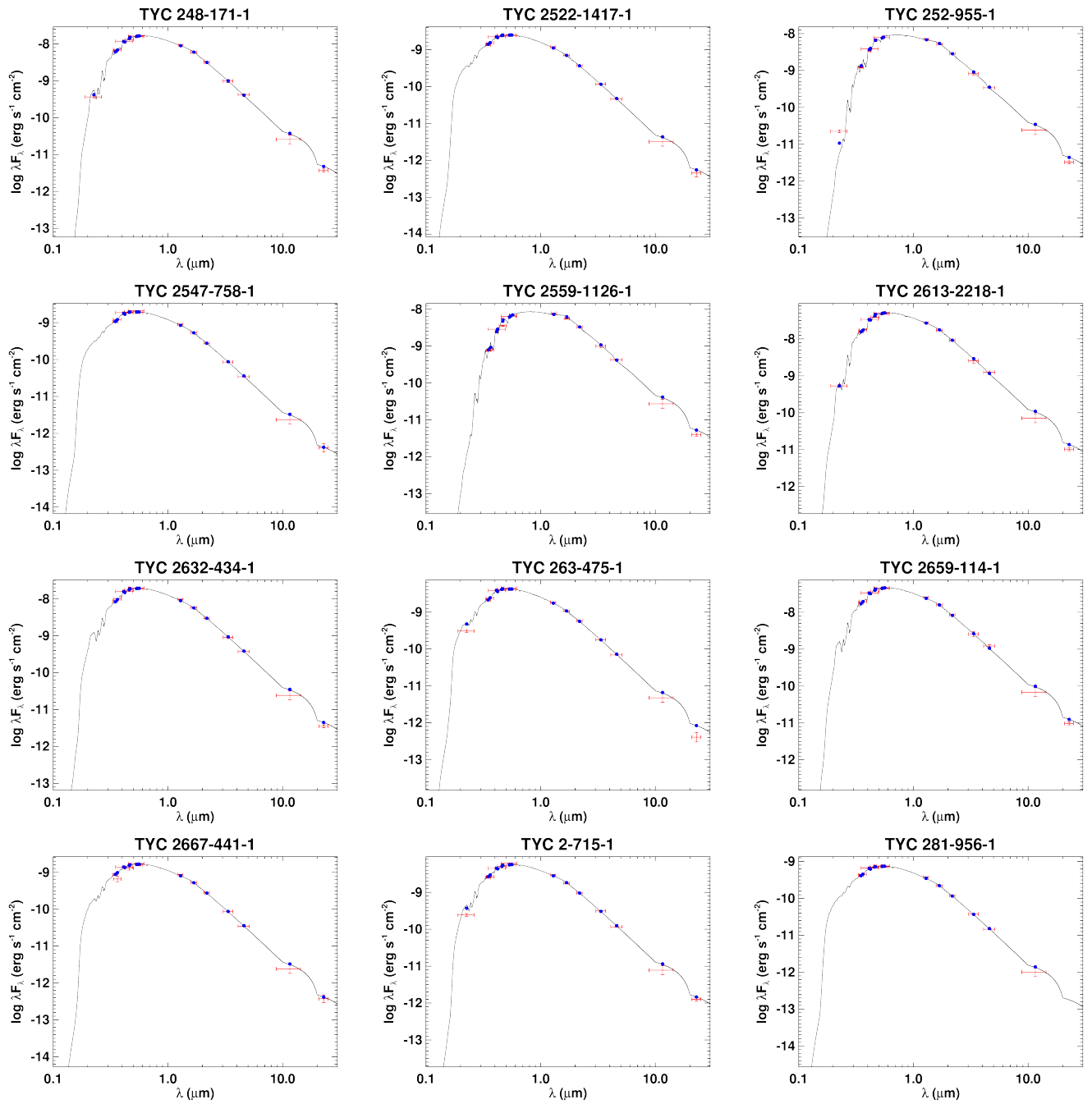


Figure A6. All labels, lines, symbols, and colors as in Figure A1.

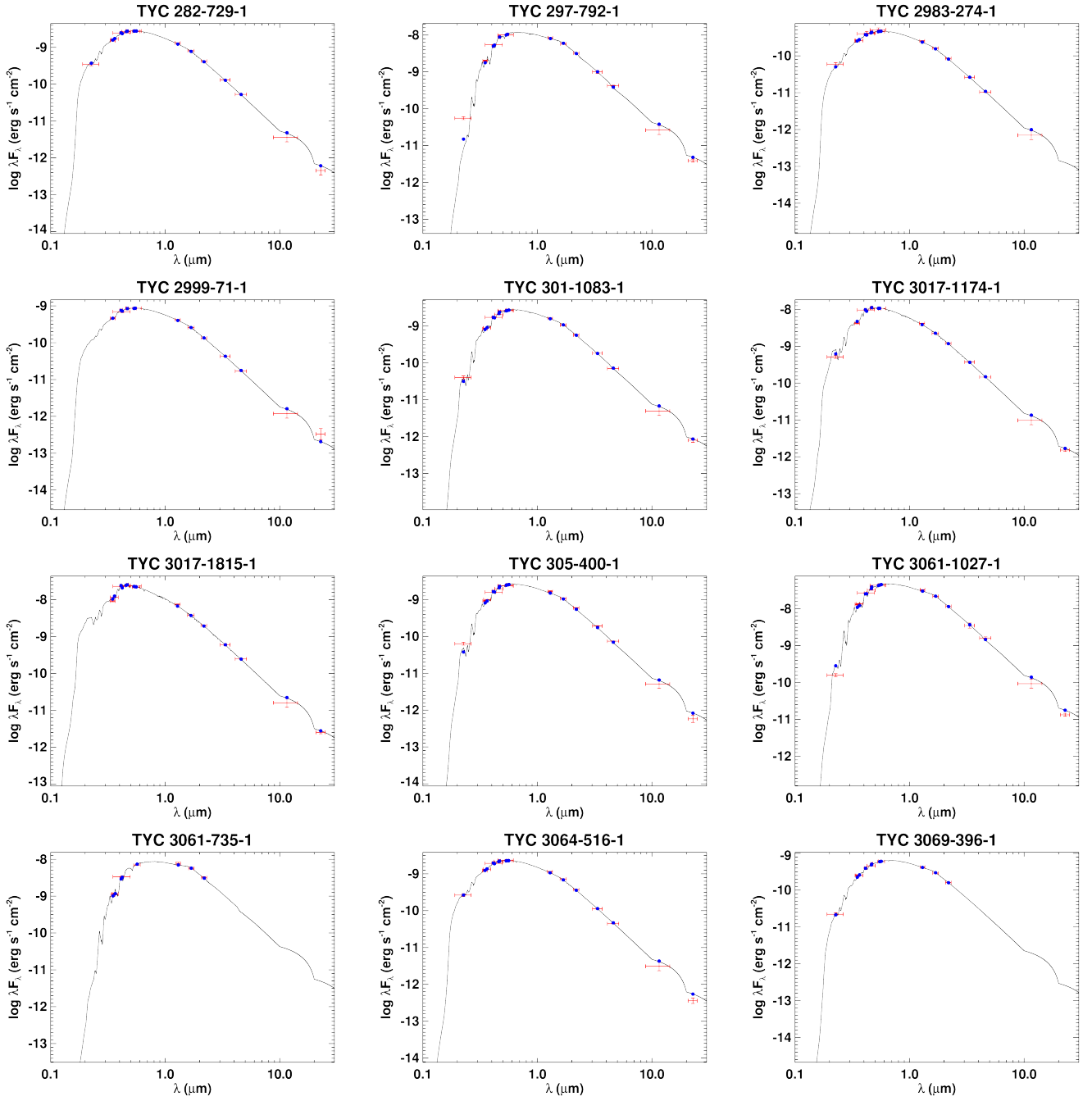


Figure A7. All labels, lines, symbols, and colors as in Figure A1.

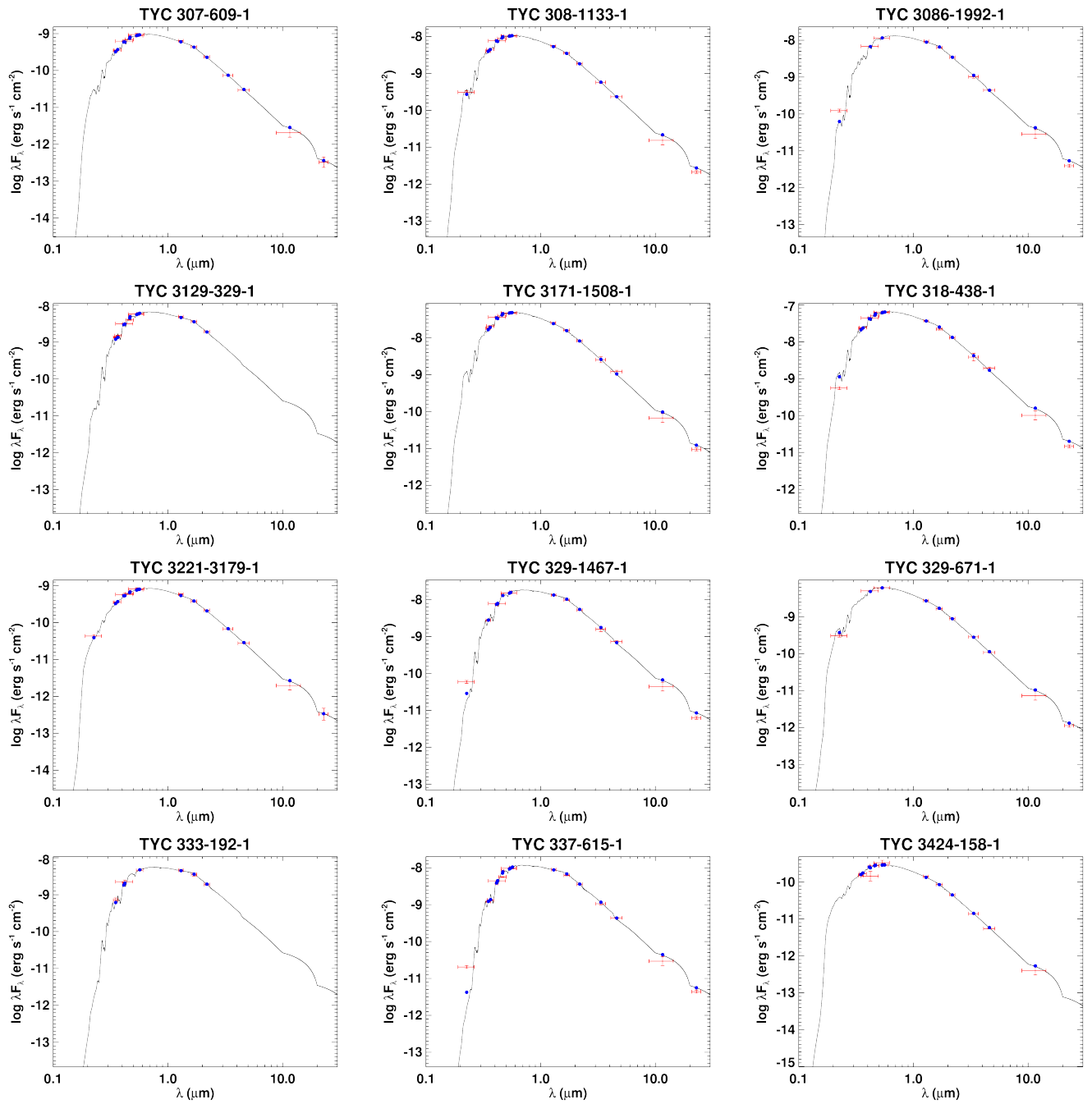


Figure A8. All labels, lines, symbols, and colors as in Figure A1.

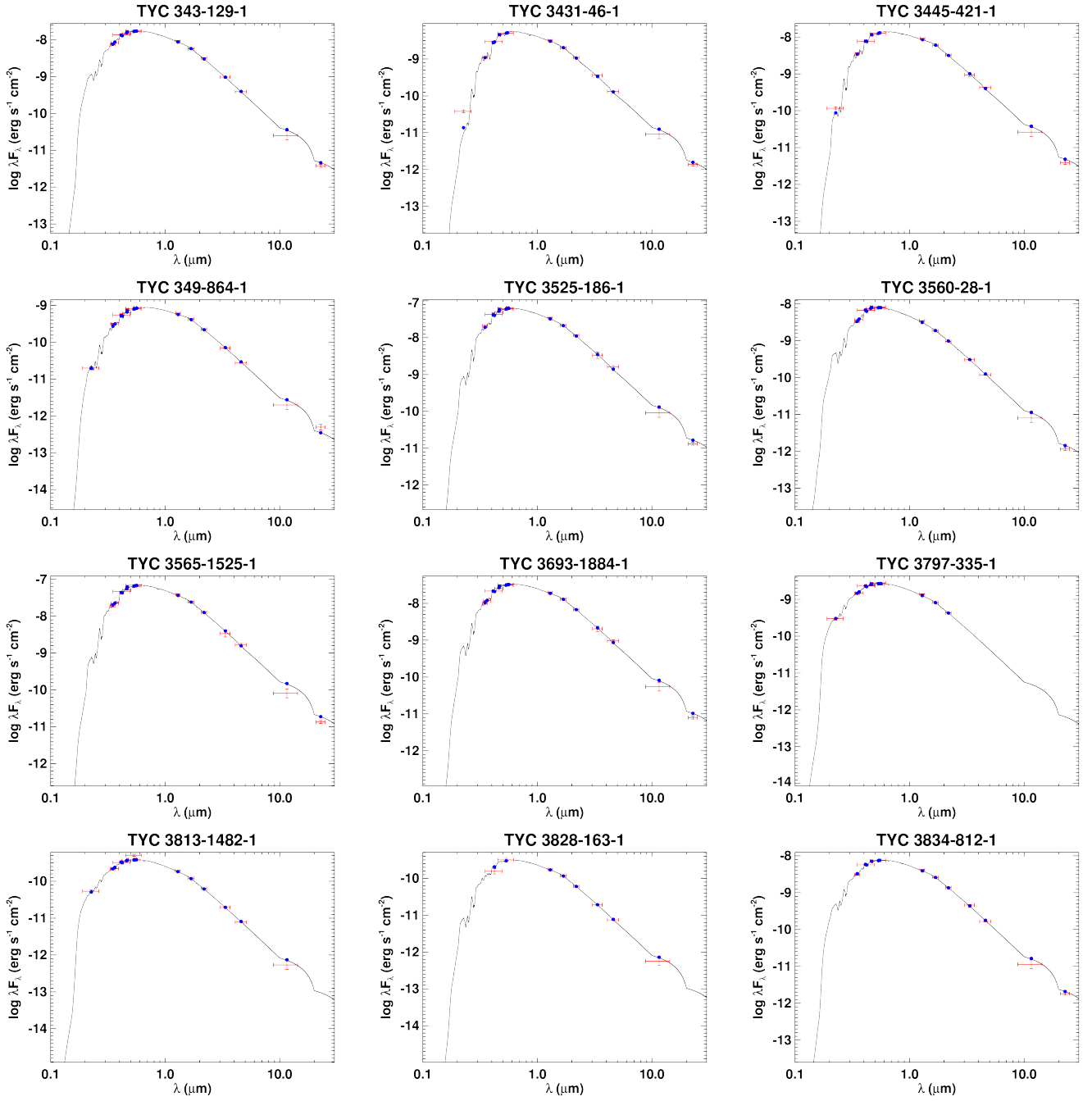


Figure A9. All labels, lines, symbols, and colors as in Figure A1.

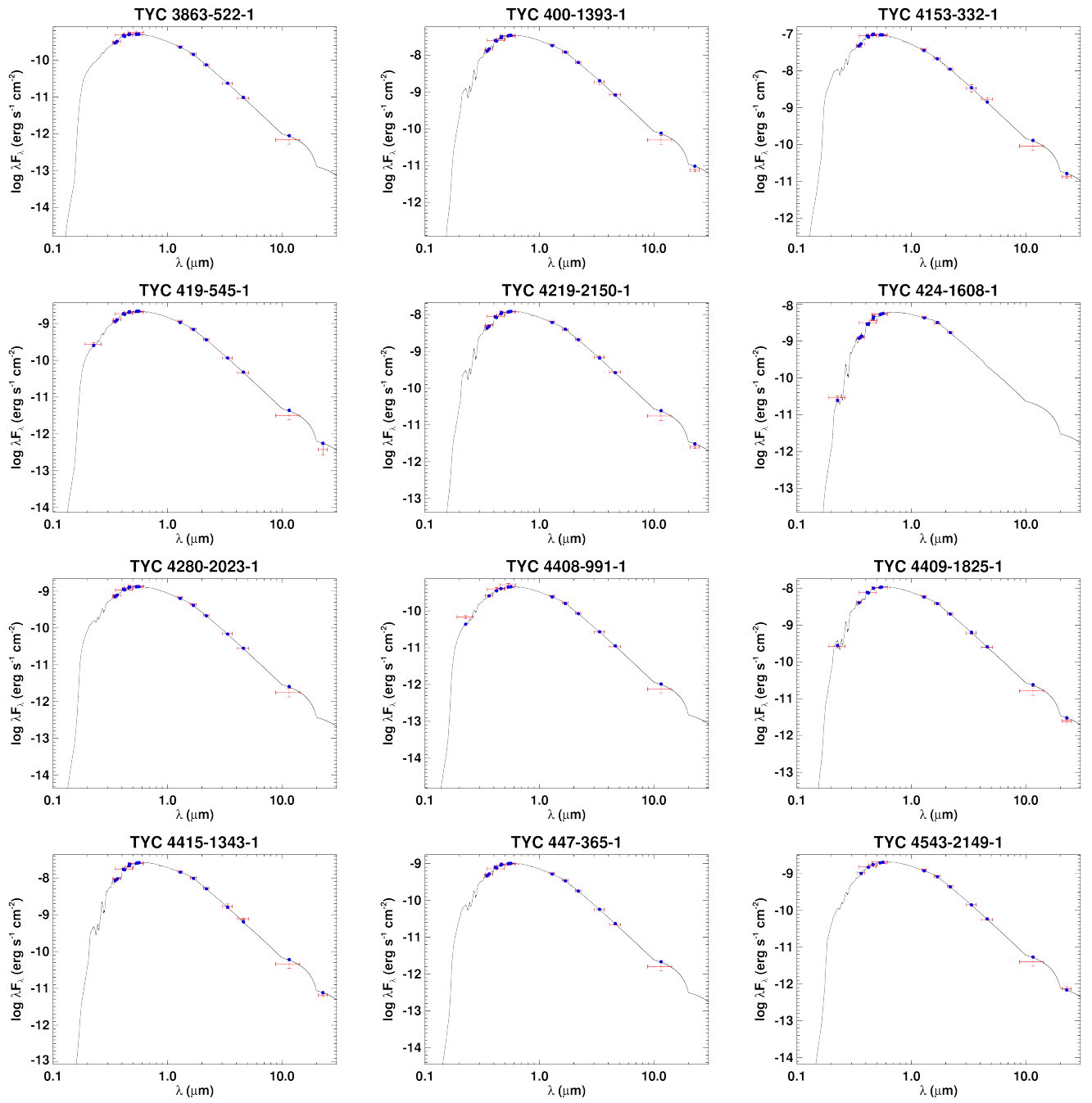


Figure A10. All labels, lines, symbols, and colors as in Figure A1.

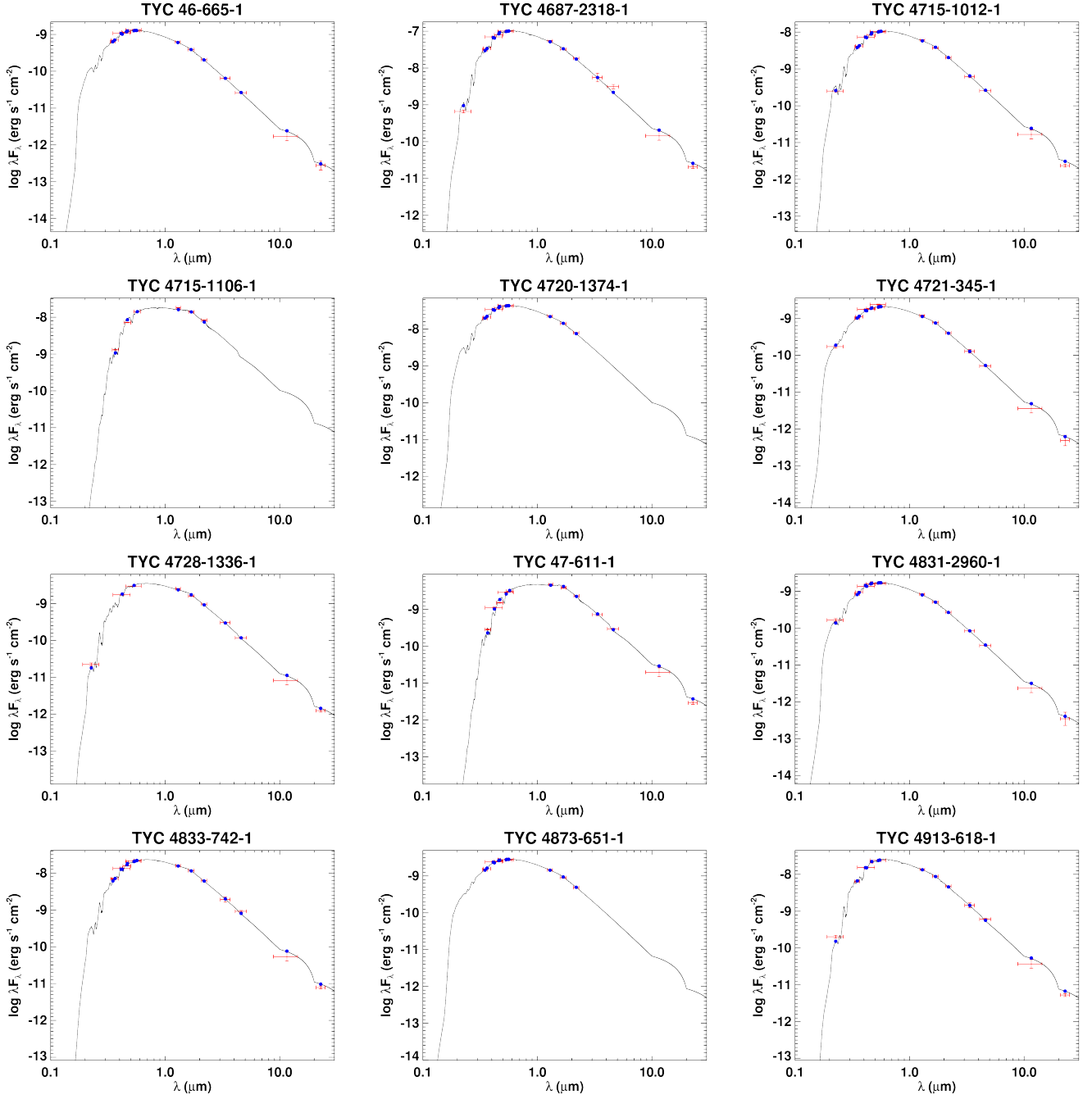


Figure A11. All labels, lines, symbols, and colors as in Figure A1.

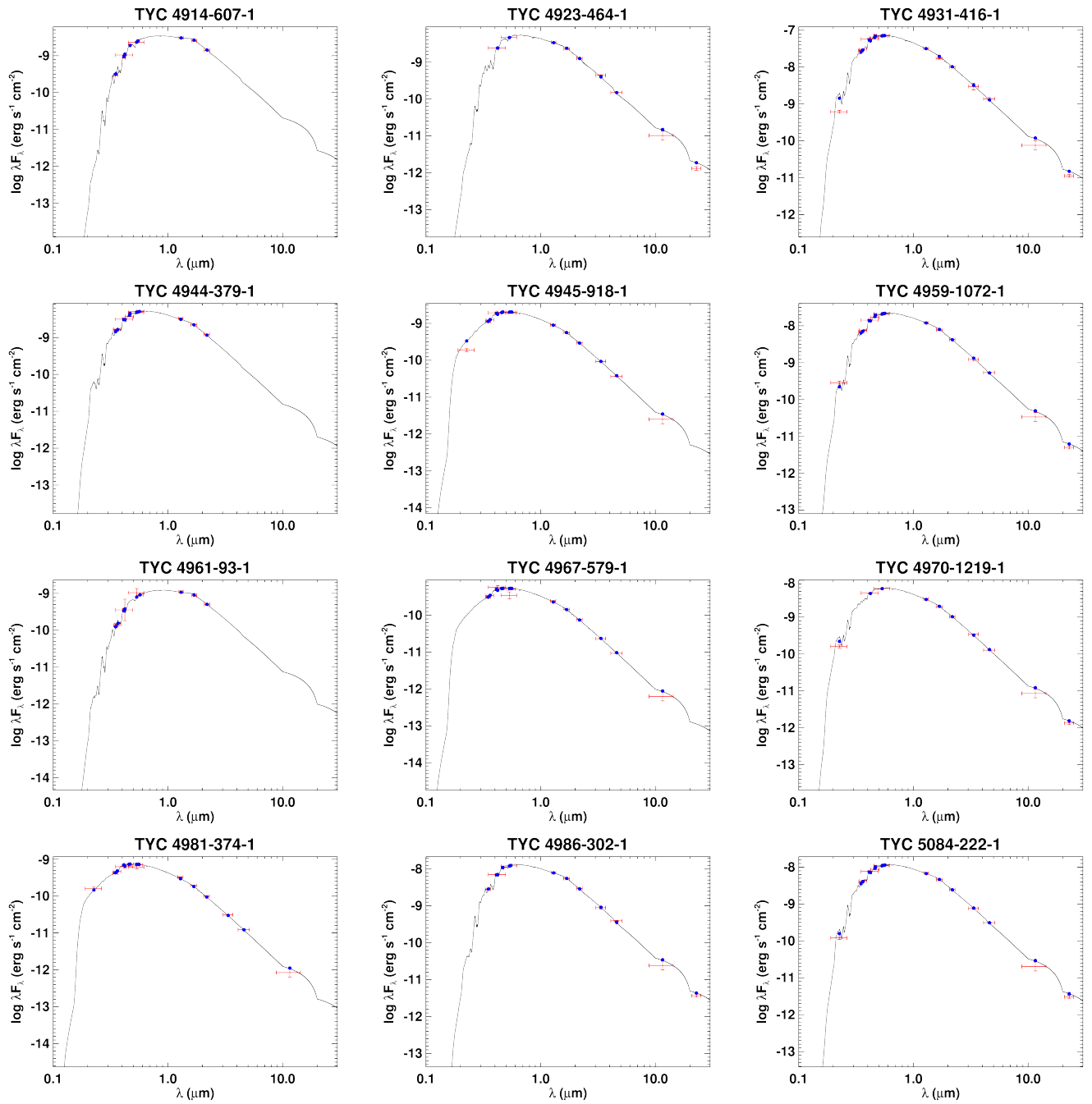


Figure A12. All labels, lines, symbols, and colors as in Figure A1.

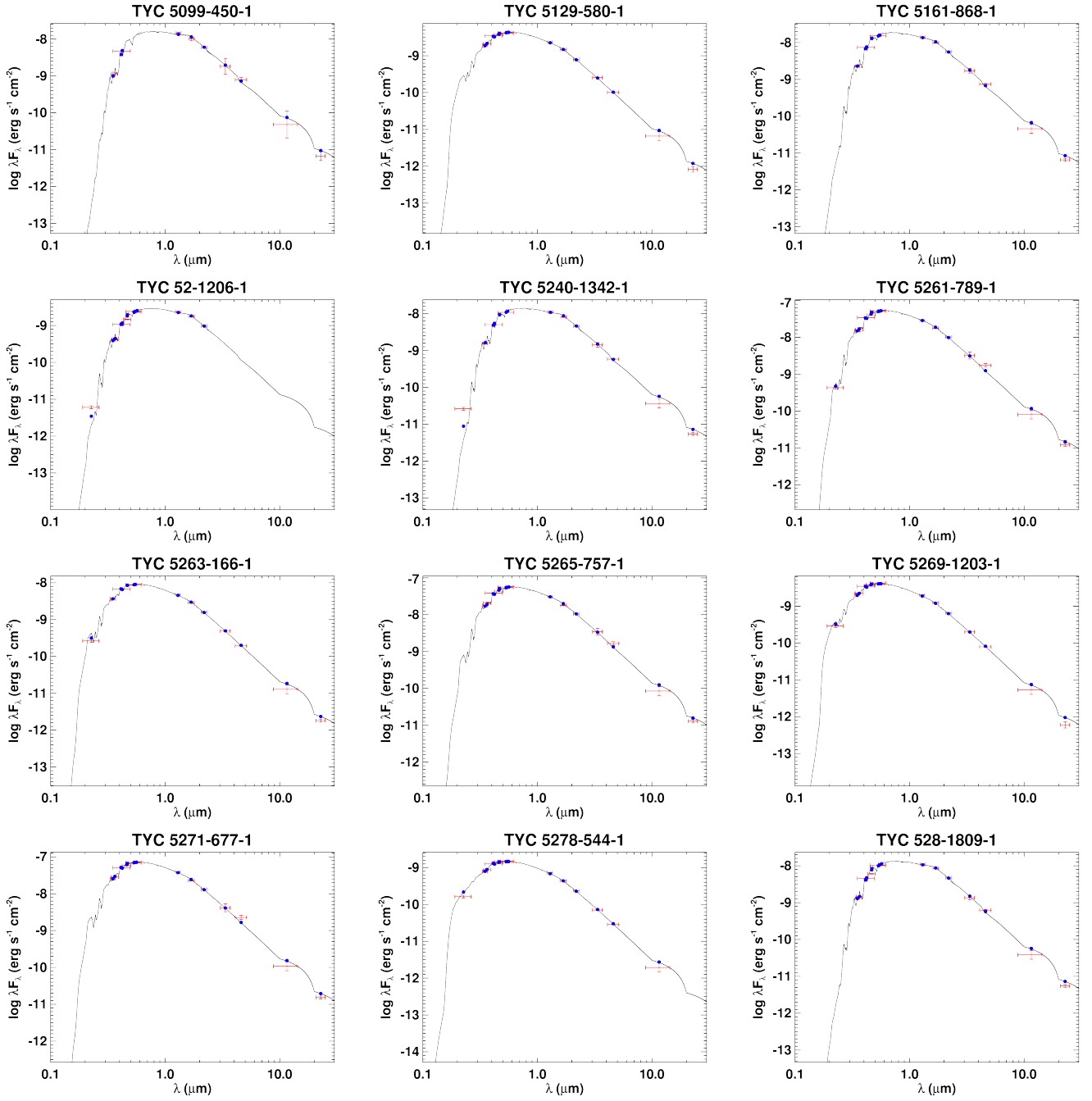


Figure A13. All labels, lines, symbols, and colors as in Figure A1.

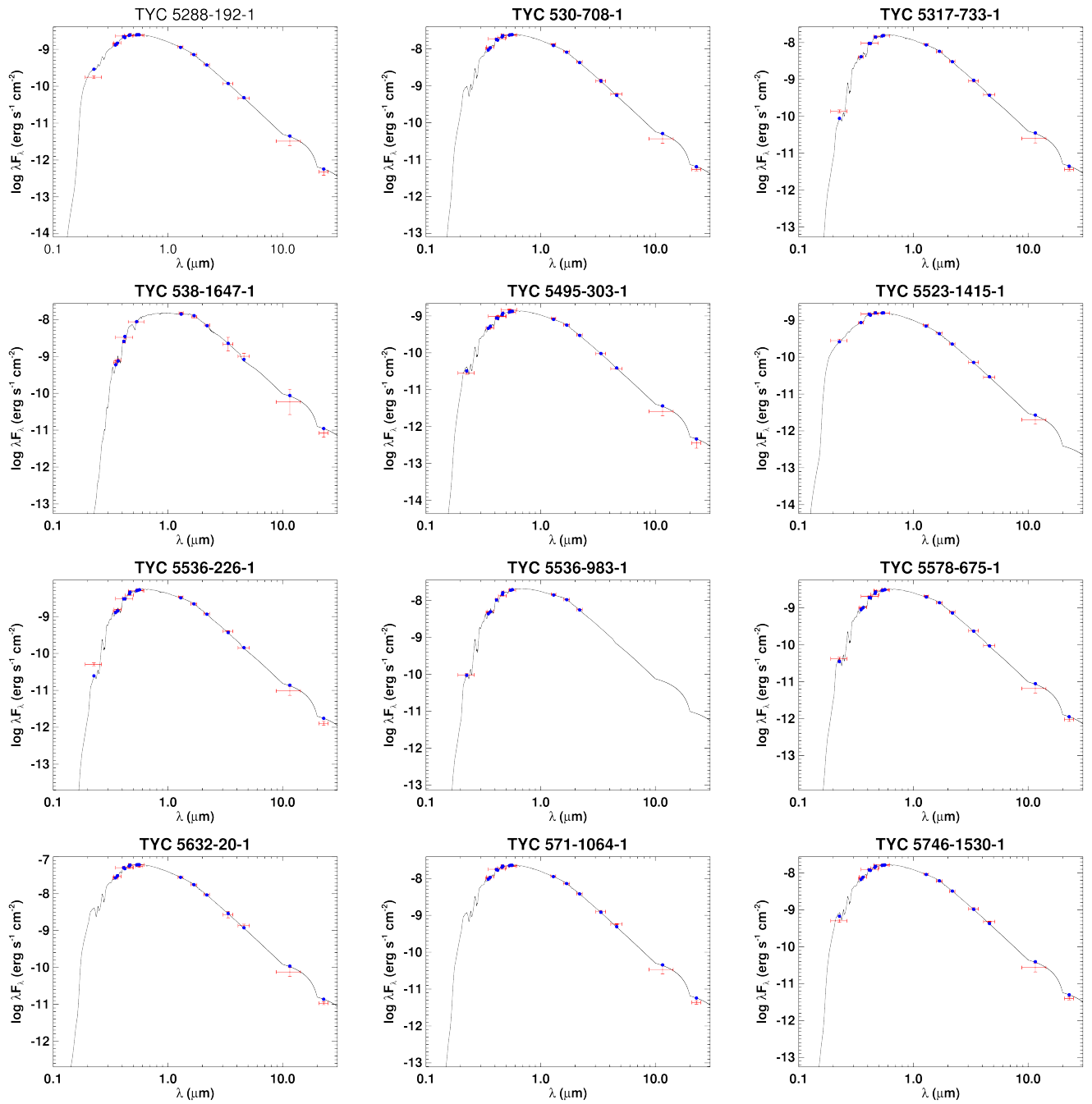


Figure A14. All labels, lines, symbols, and colors as in Figure A1.

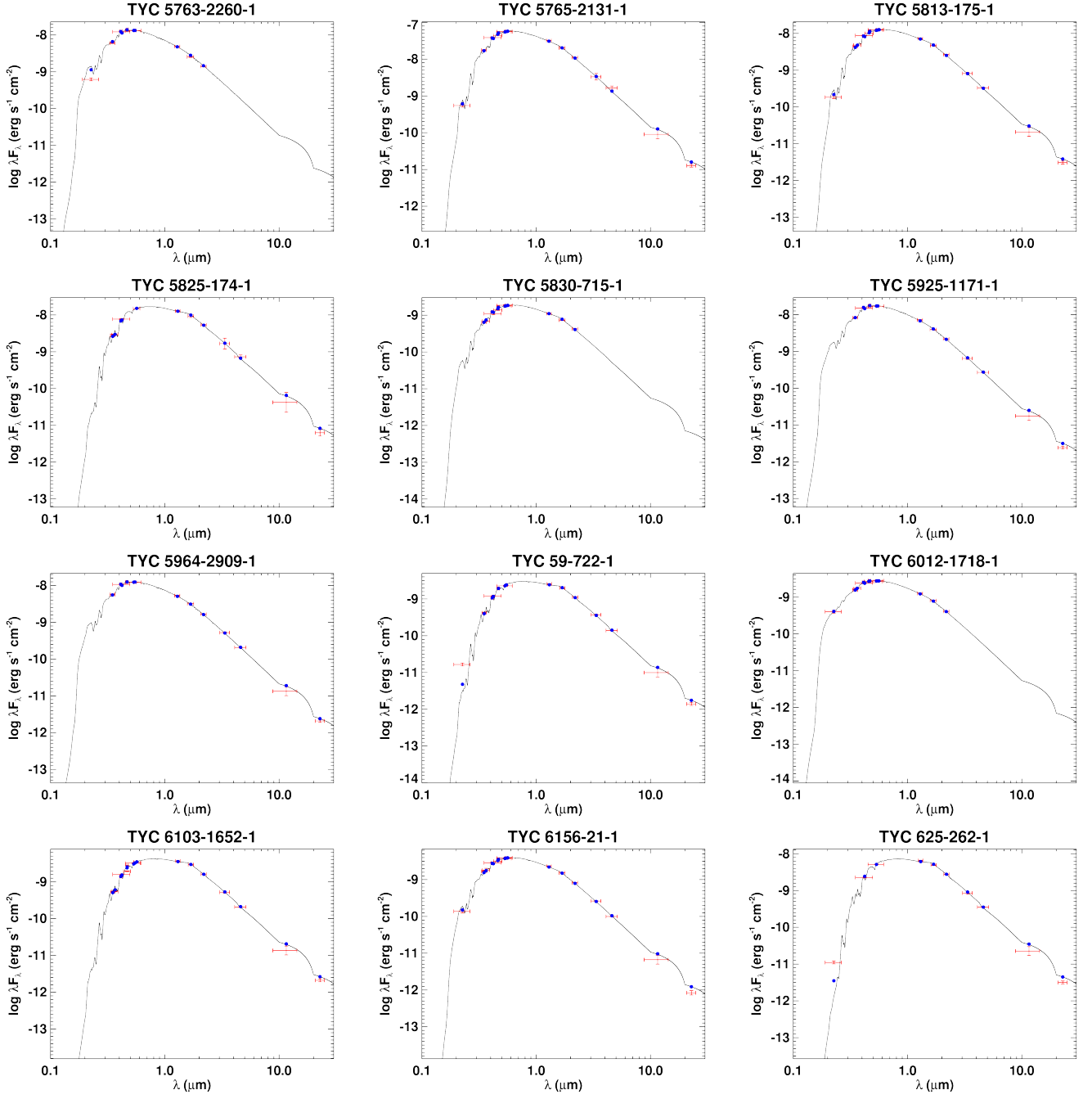


Figure A15. All labels, lines, symbols, and colors as in Figure A1.

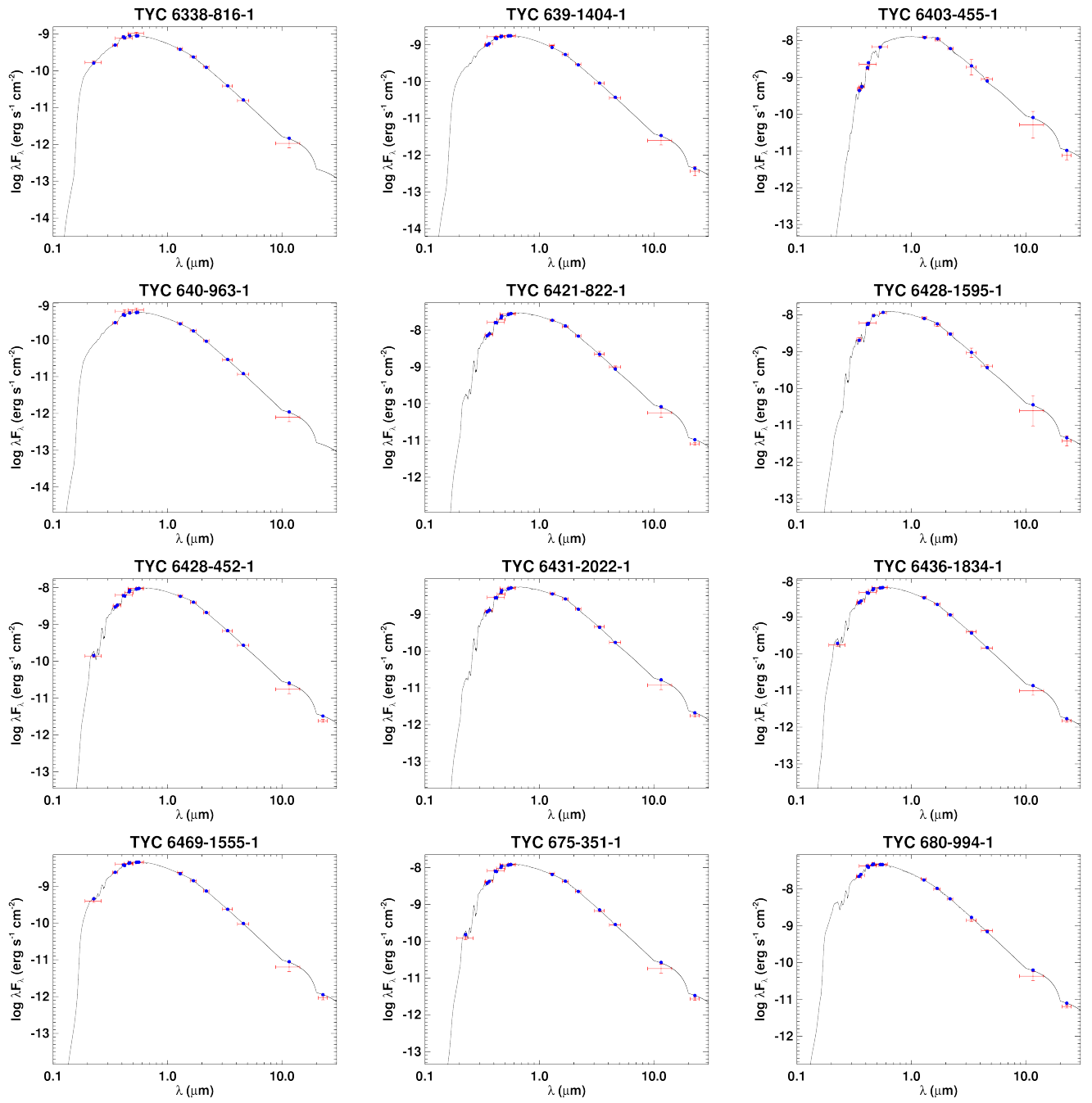


Figure A16. All labels, lines, symbols, and colors as in Figure A1.

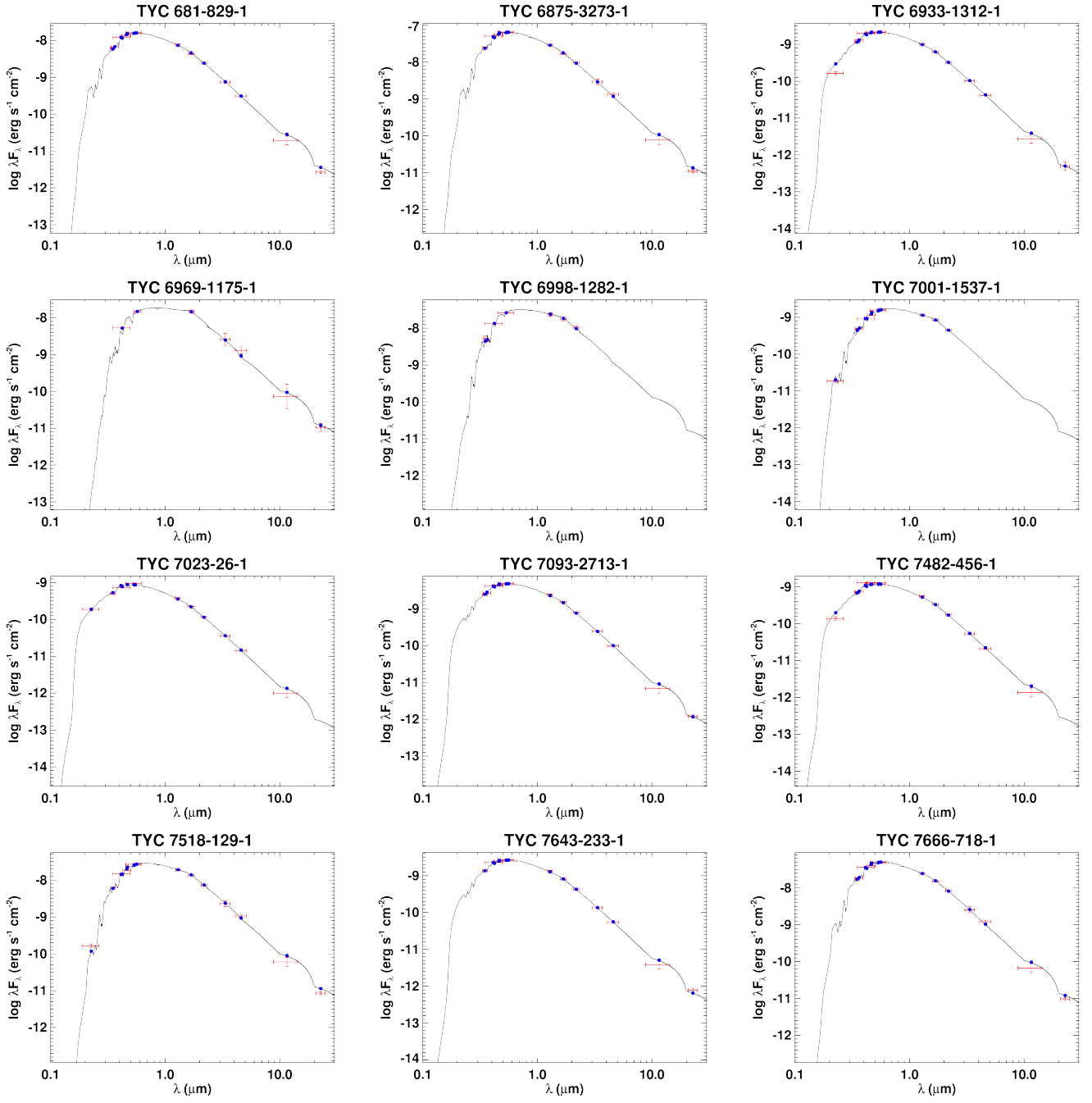


Figure A17. All labels, lines, symbols, and colors as in Figure A1.

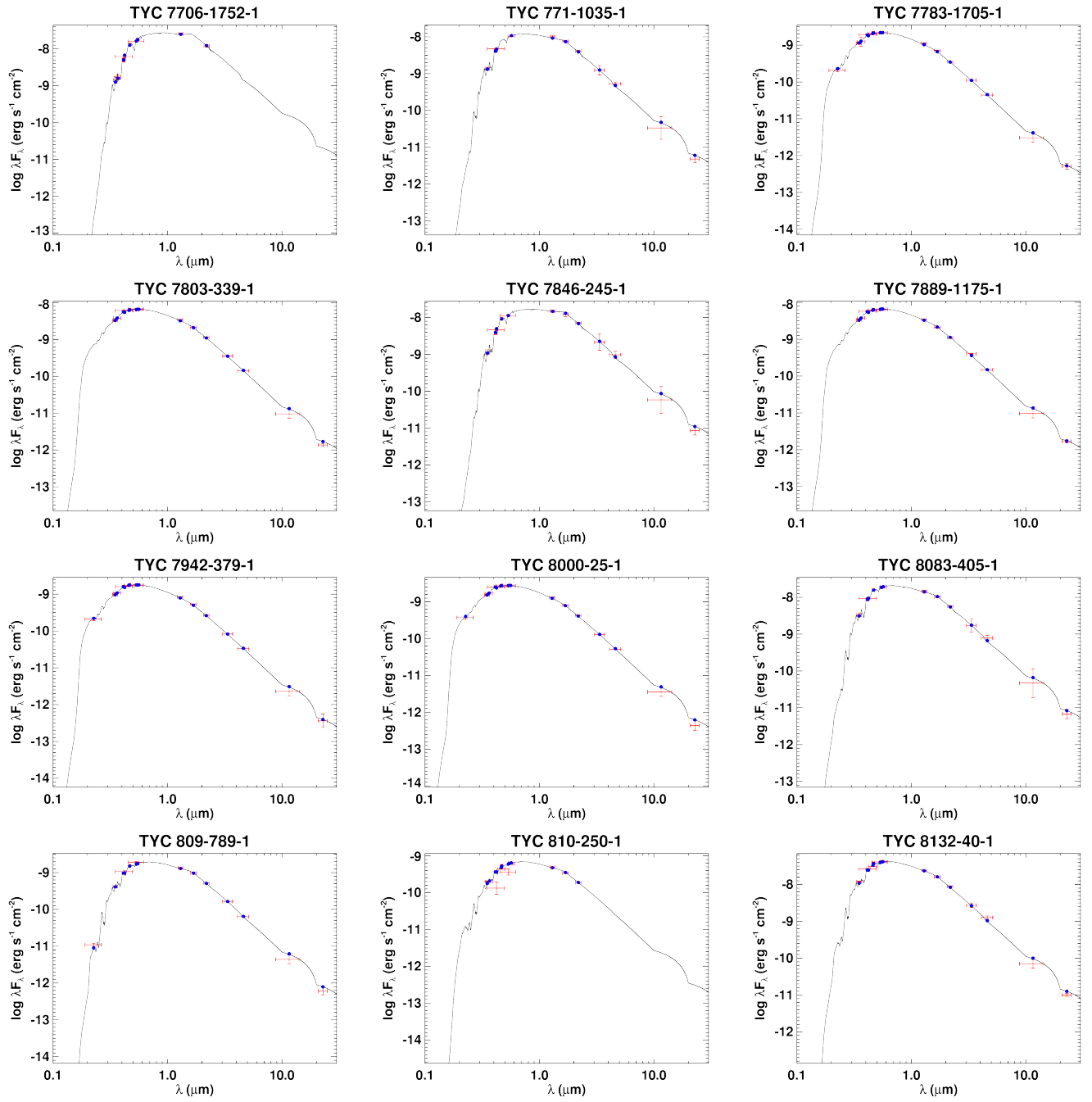


Figure A18. All labels, lines, symbols, and colors as in Figure A1.

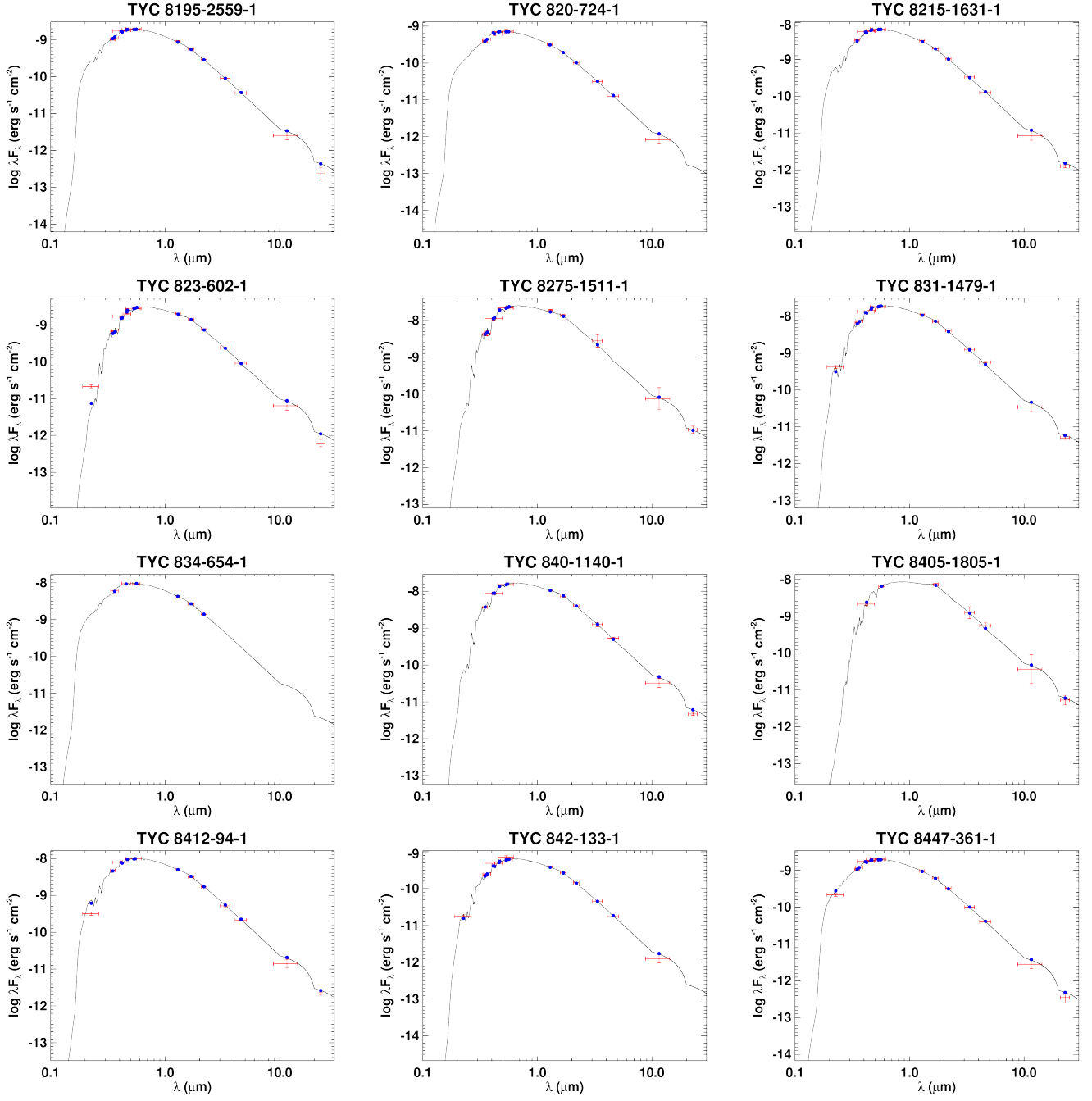


Figure A19. All labels, lines, symbols, and colors as in Figure A1.

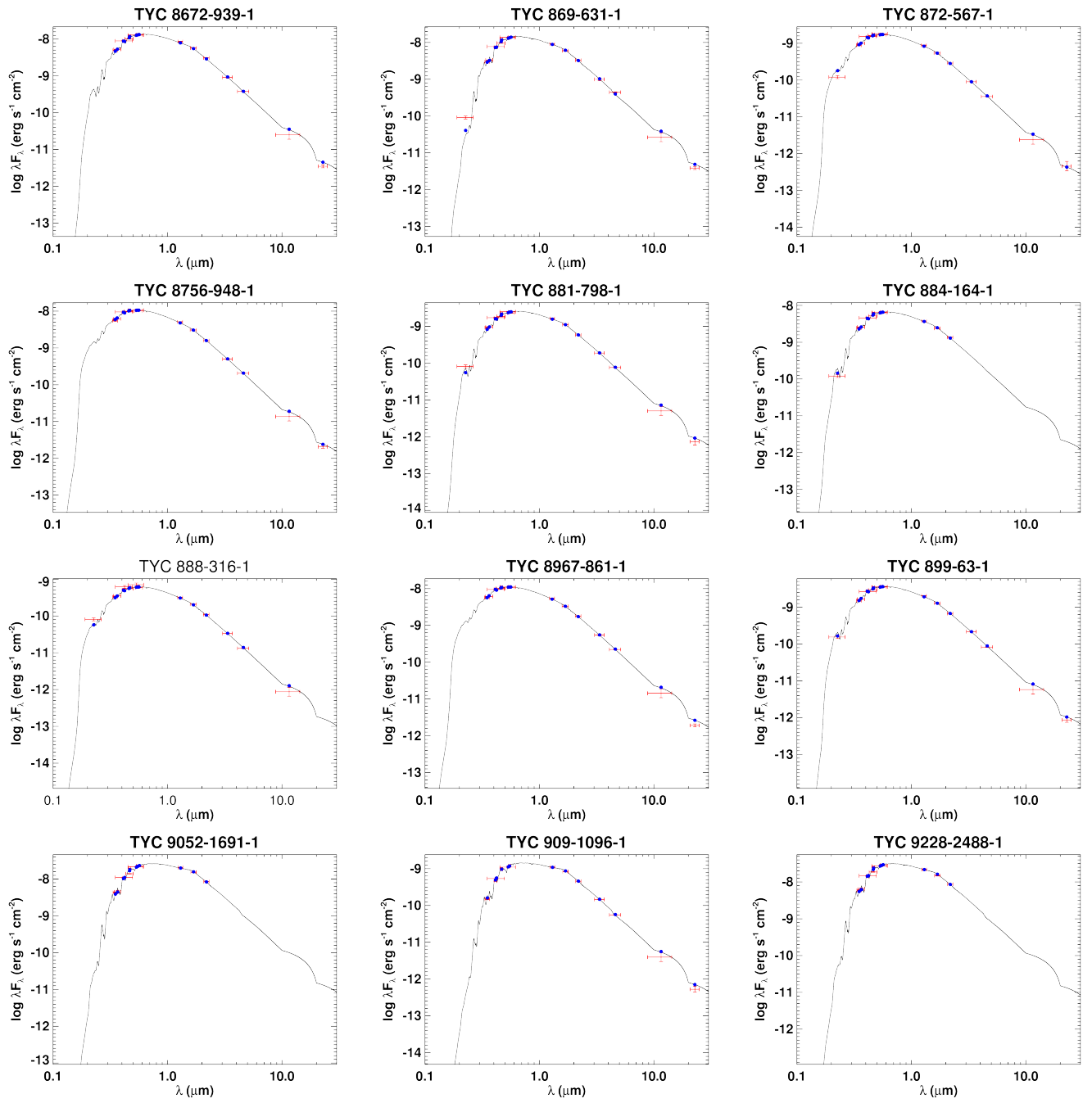


Figure A20. All labels, lines, symbols, and colors as in Figure A1.

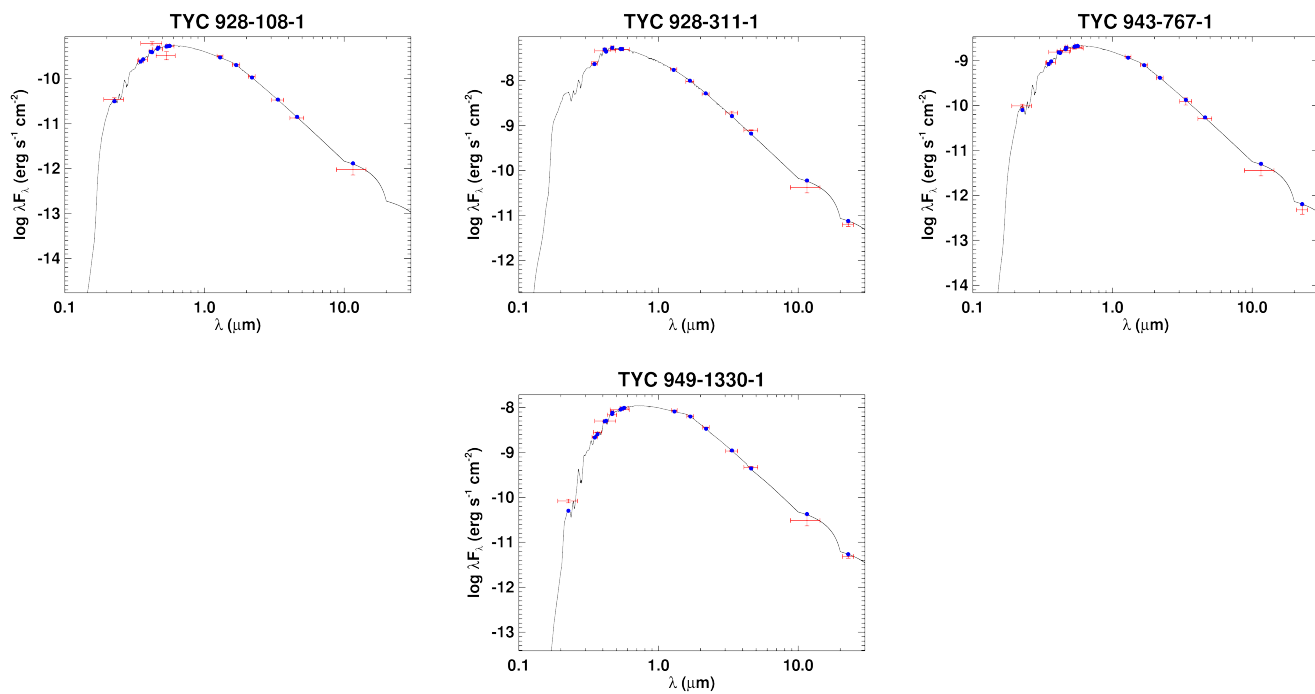


Figure A21. All labels, lines, symbols, and colors as in Figure A1.